Politecnico di Torino

ScuDo
Scuola di Dottorato ~ Doctoral School
WHAT YOU ARE, TAKES YOU FAR

Doctoral Dissertation
Doctoral Program in Computer and Control Engineering (35^{th}cycle)

Study and Implementation of Compact Modeling Techniques for the Energy Analysis and Optimization of Complex Systems

By

Alberto Bocca

******

Supervisor(s):
Prof. Enrico Macii, Supervisor
Prof. Alberto Macii, Co-Supervisor

Doctoral Examination Committee:
Prof. Luca Benini, Referee, ETH Zürich, Swiss, and Università di Bologna, Italy
Prof. Mircea R. Stan, Referee, University of Virginia, USA
Prof. Andrea Calimera, Politecnico di Torino, Italy
Prof. Emanuele Lattanzi, Università degli Studi di Urbino, Italy
Prof. Graziano Pravadelli, Università degli Studi di Verona, Italy

Politecnico di Torino
2023

Declaration

I hereby declare that, the contents and organization of this dissertation constitute my own original work and does not compromise in any way the rights of third parties, including those relating to the security of personal data.

Alberto Bocca
2023

* This dissertation is presented in partial fulfillment of the requirements for **Ph.D. degree** in the Graduate School of Politecnico di Torino (ScuDo).

I dedicate this thesis to the living Lord for blessing me to accomplish the impossible, and to my beloved family

Acknowledgements

There are always many people to thank when an important goal is achieved.

In the first place, my dear mother, whose example, sacrifices, and prayers of faith had a great influence on the results I achieved in all the years of study at the Politecnico di Torino. She supported me in all my tasks and always trusted me. This attitude was one of the main reasons I was able to complete this PhD program. I am also very grateful to my dear father for his support and the sacrifices he made for me and his family during my previous studies, which made it possible for me to get here. In addition, I must commend my sister Maria Teresa, who has always encouraged me and has always stood by our family when needed.

Great thanks are due to Prof. Enrico Macii for his continued trust, his great talents and skills in the field of research, and his exemplary gratitude.

I am very grateful to Prof. Alberto Macii for his high respect and kindness towards others, his constant support for my research, and his inspiring suggestions.

I would also like to thank Prof. Massimo Poncino for his relevant collaboration and remarkable observations regarding my research, which even led to the improvement of several manuscripts. Great thanks are due to Prof. Donkyu Baek for always believing in the ideas I shared with him and for the articles I published during these years of collaboration with him. Many thanks to Yukai Chen and Wenlong Wang for their significant contribution to battery performance research.

Finally, but not least, special thanks to Alberto Catalano (Università di Torino) for his valuable advice in the statistical analysis of data.

Great gratitude is due to each person who has sustained me during these years.

Abstract

In an increasingly rich world of complex systems (e.g., in physics, biology, economics, and social sciences), the general trend is to analyze and predict certain phenomena using accurate models (e.g., neural networks) that are also complex. For this reason, apart from the basic structure, such models are neither easy to build nor to understand in all details, as they often require many functions and a large number of coefficients, mathematically speaking, even significant computational resources. Instead, this work attempts to restore simplicity by defining compact models that are easy to use, considering energy as the application area of this research. In particular, the models described in this document concern battery consumption, efficiency in the use of a network of electric vehicle charging stations, and solar energy analysis.

Regardless of whether the initial modeling approach is purely mathematical or programming-based, the real goal is always to obtain simple analytical expressions that can satisfactorily describe the characteristics of the processes and systems under test. Although it cannot be assumed that there is a compact model or a general solution for every complex system, the research results confirm that in several cases it is possible to create compact models that are more practical to use. In this way, a larger number of people can access the basic analysis of the available data in a given scenario. The creation and sharing of such models allow a better understanding of the phenomena under consideration, in particular the identification of the parameters that most influence the overall behavior of a given system and the degree of their correlation with it.

Before describing the applications, general guidance is given on the compact modeling method used here. Then, the accuracy of the proposed models is analyzed by comparing the results with those obtained with more sophisticated methods and tools or directly with experimental data.

Contents

List of Figures

List of Tables

Chapter 1

Introduction

1.1 Emergent complex systems

Complex systems can be divided into systems of disorganized complexity and organized complexity [2]. In the first case, statistical methods are commonly used to determine the probability of certain events, for example in the case of systems when the number of variables is very large and each variable exhibits an erratic behavior. In the second case, there is an interrelationship between the elements, which indeed operate as a whole.

This world is full of complex systems, both natural and artificial, in which many elements, also called agents, interact with each other in collaborative ways and with their own dynamics, such as ecosystems in ecology, stock markets, and the traffic of vehicles among others [3]. One of the most important properties we find in most such systems is self-organization, i.e., the property of elements to coordinate themselves to achieve a stable state of the system [4]. Nowadays, correspondences between such systems with a self-organizing property and quantum dynamics are even reported in the literature [5].

As a definition, Nino Boccara has written that a system that "consists of large populations of connected agents... is said to be *complex* if there exists an emergent global dynamics resulting from the actions of its parts rather than being imposed by a central controller" [6]. On the other hand, if the elements of a system (e.g., computer) work together for a certain known function, then this system is in fact only complicated [7].

In this scenario, the term *emergent* refers to the properties of the behavior of a collective agent when it differs from the behavior of a single agent [6]. Accordingly, it is possible to find complex systems in many domains, as shown in Figure 1.1.

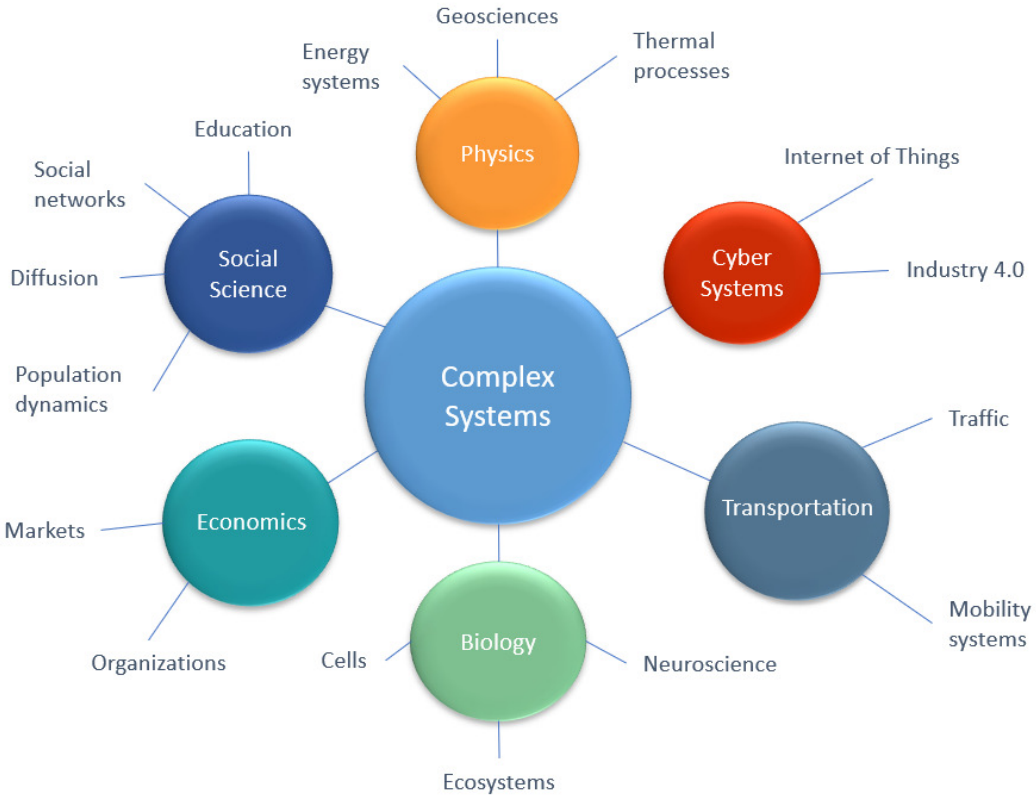

Fig. 1.1 Major areas of interest for complex system analysis.

In general, there was a barrier in the past that seemed to prevent the creation of accurate models of the complex systems that were being created. For example, in [8] the authors claimed the following: "Emergent complex systems... cannot be fully explained mechanistically and functionally". Furthermore, in [9], the author stated: "Emergent behavior is not sufficient to characterize a complex system". Nowadays, however, characterizing emergent behaviors through novel modeling techniques can lead to the ability to simulate and predict with the greatest accuracy possible situations that arise from such systems. Indeed, both mathematical and computational models have recently been developed in this area [6, 10]. Neural networks, for example, have improved the accuracy of forecasts (e.g., for weather). However, they usually have many coefficients, even hundreds, depending on the number of inputs, nodes, and connections [11]. On the other hand, Hiroki Sayama

affirmed that a “good model is simple, valid, and robust” [12]. Consequently, studies on compact models for emergent complex systems are still ongoing, especially in terms of developing a common methodology for developing these models in different scientific fields.

1.2 Modeling complex systems

Although there are detailed descriptions of model building processes in the literature [13, 14], this thesis focuses on some simple techniques that can potentially be used to compactly model the emergent behavior of these systems. In general, there are two different approaches to building models:

- developing new models
- modifying and adapting existing models.

The latter also includes the adoption of models from different application areas. Certainly, developing new models is a very challenging task for a researcher trying to describe or predict phenomena and processes. The goal of creating a compact model adds to this challenge. For this reason, the most common modeling approach is to extend or reduce existing models. Indeed, it is certainly easier to improve existing models than to create entirely new models that differ from those described in the literature. Finally, adopting models from different application domains, sometimes with some tricks or precautions, is another solution for modeling [15]. In addition to these general approaches, modeling can be based on two different methods:

- theoretical modeling
- empirical modeling

The first method considers the physical/chemical laws for building models based on the theory (i.e., the “first principles”) of these laws and the associated parameters, while the second is based on data analysis and therefore generally follows a purely statistical approach, which nowadays includes machine learning techniques (ML). In the latter case, the analysis of time series data is one of the most common approaches to develop predictive models (e.g., for energy consumption forecasting) [16, 17].

Hybrid methods involving a combination of "first principles" and ML techniques are also commonly used in modeling [18, 19].

To understand the fundamental causes of certain behaviors of a system, good questions are essential to finding the answers that lead to the phenomena that characterize a complex system [20, 21]. For example, "Why were certain results obtained in the tests/simulations?" or "What boundary conditions or states of the system parameters lead to different behavior than expected?"

1.2.1 Mathematical modeling

Since the interactions between elements in a complex system generally have nonlinear features, these interactions are usually described by a set of equations, in particular ordinary and partial differential equations (ODE and PDE, respectively) [6, 22]. Reduced-order models can be useful, but they are generally less accurate [23]. Principles and guidelines for mathematical modeling can be found in [20].

Nowadays, a statistical approach is usually used for feature extraction in the context of data series and databases. Among the best-known methods are those of regression and those based on Bayesian statistics [24]. The approach taken in this document is somewhat different. For example, although the construction of regression models is still based on physical parameters and coefficients, the proposed approach may involve not only a purely statistical preliminary analysis of the collected data (e.g., analysis of covariance), but also consider theoretical aspects to generate the interaction terms of a mathematical model. Results will show that such an approach can lead to better accuracy.

Although a description of *emergent* behavior in complex systems could have been questioned in the past as a comprehensive account of these systems, Yaneer Bar-Yam "argue[s] conceptually and then demonstrate mathematically that it is possible to define a scientifically meaningful notion of strong emergence" [25]. This thesis tends to confirm this assumption by presenting models that describe such behaviors analytically, rather than being limited to describing individual properties and interactions of elements. Moreover, the attempt to create compact models is essential for a wider audience to understand and analyze the global behavior of certain phenomena.

1.2.2 Computational modeling

Currently, there are several tools to model complex systems computationally. For *system dynamics*, which is a more general description of the interactions of elements, some of the best-known are Vensim® [26], Powersim Studio [27], and Stella® [28]. These tools generally do not require the user to write any program code. In contrast, agent-based modeling tools allow a description of the specific behavior of each element in a system; however, these tools generally require program code. In this case, some of the most common tools are NetLogo [29] and AnyLogic [30] which allow both system dynamics simulation and agent-based simulation. Although some of the existing modeling software tools are freely available in an educational version, it is also common today to develop agent-based models using open-source software such as FAME (open Framework for distributed Agent-based Modeling of Energy systems) [31], Repast [32], and MESA [33], among others.

System dynamics is based on the description of the behavior of a population of elements, or agents, as a whole [34]. The definition of these models is usually based on the general rules that regulate the dynamics under consideration. For this reason, system dynamics models are expected to be simpler than agent-based models (ABMs). However, they often become so extensive with many variables and functions that they do not analyze complex systems as compact as would be desirable.

This is only a general overview of the state of the art in software tools for modeling complex systems, as a more comprehensive analysis is beyond the scope of this document.

1.2.3 Developing compact models

At the beginning of this century, in [35] it was claimed that a general model for complex systems is not possible. Today, however, machine learning techniques, especially neural networks, can enable the creation of accurate models [36, 37], especially for identifying the parameters (e.g., descriptors) that mainly influence the behavior of systems and processes [38]. In addition, identifying the dependence of the different states in a complex system can also lead to building a more compact model [39].

In [40] the author divided complexity into three distinct branches: *algorithmic complexity*, *deterministic complexity*, and *aggregate complexity*. Algorithmic complexity deals with system properties from a mathematical and information-theoretic perspective. Deterministic complexity deals with chaos theory and catastrophe theory, while aggregate complexity deals with the agents of a system, their behavior, and their interactions with each other. Accordingly, the method for modeling complex systems, as presented in this thesis, includes the first and last domains of analysis.

In this thesis, the basic approach to building new compact models is mostly based on a correct understanding of the *emergent* behavior of the complex system under consideration and the correlation analysis of the system variables affecting this behavior. This analysis can generally be performed by considering (i) a multivariate domain in which the variables that best describe the expected system response are selected, or (ii) the overall function describing the general outcome from the simulation of an extensive model (e.g., ABM).

For the first case, Figure 1.2 shows the adopted logical flow in selecting the variables and the loop for the generation of a new compact model with an expected accuracy. In this case, the preparatory step is based on the correlation analysis to select *n predictor variables* to be included in the model, from a set of *m* variables [41]. In this context, the selection of variables is done by analyzing the coefficients ρ of the Pearson correlation matrix, which includes the coefficients of the correlation between the input variables X and the output variable Y (i.e., the *response variable*), and those related to each pair of the input variables. The variables that have a high correlation coefficient are then selected from the entire data set. More specifically, the selection is made based on whether the output $\rho_{x_i,y}$ (with i ranging from 1 to m) is greater than a threshold ρ_{t1}, or the correlation coefficient with another input variable ρ_{x_i,x_j} (for i$\neq$j) is greater than a threshold ρ_{t2}. The two thresholds ρ_{t1} and ρ_{t2} can be set differently since the criterion for selecting the variables for the two cases of correlation (i.e., with the output variable and with the other possible input variables) can thus be distinguished. Starting from all the selected variables, models with different interaction terms are built one after the other. The definition of these terms is the most challenging part of this modeling approach. Indeed, the interaction terms may consist of a single variable or joint variables, and each term and each variable may have a different degree and include different functions (e.g., exponential, trigonometric, etc.).

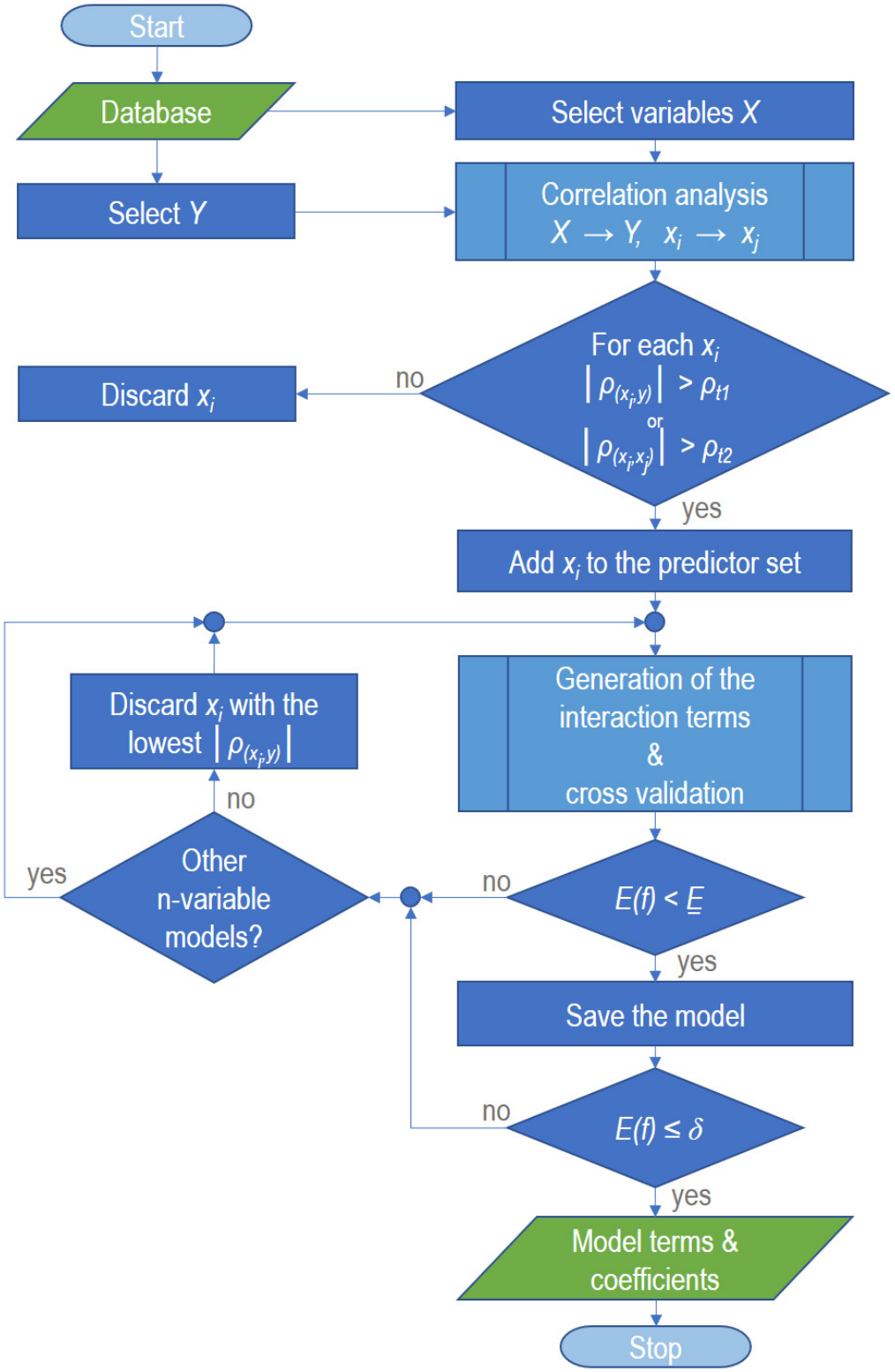

Fig. 1.2 Flow chart of the methodology for the predictor variables and model selection.

Each model is then tested with the cross-validation method. If the error $E(f)$ of the model function under test is less than the lowest error $\underline{E}$ found during all the previous tests for other models, then the current model is saved. Furthermore, if the error is such as to guarantee the desired accuracy δ, then the model could be considered the definitively approved one. However, in case such accuracy is not obtained from the models with all the variables selected at the beginning, the variable with the weakest $\rho_{x_i,y}$ is discarded from the set of variables. So on until eventually generating models with only one variable. In any case, the total number of variables selected (i.e., generally $n \leq 4$), as well as the number of coefficients, must be limited so that a model can still be considered a compact model. The above procedure can be adapted, depending on the data considered for modeling, by using nonparametric rather than parametric tests such as the Pearson correlation test.

On the other hand, the simulation results of an ABM for a given system should be collected and analyzed in terms of the appearance or behavior to focus on. In this case, the attention in advance must be mainly on the aspects of the system to be analyzed or optimized and not on the model, which instead should be considered in detail only in a second step.

The models described in this document are generally of the polynomial or rational type. They can be adapted, simplified, or new models compared to those described in the literature.

1.3 Energy analysis and optimization

Due to technological change and development in most countries, energy is now one of the most important concerns worldwide. In particular, the need to reduce pollution is directing research towards the use of energy resources that are alternatives to those based on petroleum products and coal, as well as reducing consumption. In addition, rising and fluctuating energy prices have also become a serious problem worldwide. For this reason, energy system modeling is particularly important for predicting available energy and consumption [42, 43], especially for management decisions at the local level and for potential investments. In this scenario, microgrids, renewables, and related facilities are currently considered [10, 23, 44]. Although there are more and more techniques and methods to predict and optimize energy consumption both

in the short and long term, most focus on the use of complex solutions instead of compact models.

For several years, various approaches have been proposed in the literature for modeling electronic components, devices, and systems that are considered complex, especially for thermal processes [45]. In this context, the basic approach for the development of compact models in the case of multiscale modeling is to consider the behavior at the system level and thus holistically [46].

Hoping to make energy analysis more understandable to the end user, the work described in the following chapters addresses (i) the modeling of batteries, whose production continues to increase with modern devices and systems (e.g., wireless sensors and smartphones), (ii) a network of charging stations for electric vehicles, and (iii) solar energy for photovoltaic applications.

Chapter 2

Battery Performance Analysis

Some of the work described in this chapter was also previously published in [47–49].

2.1 Adapting Peukert's law

2.1.1 Background and related work

In the energy sector, one of the most populated areas by researchers is that of batteries. This is a consequence of the recent impressive increase in the global production and sales of mobile devices and systems (e.g. smartphones and electric vehicles). As a result, battery performance modeling has also received much attention in recent decades [50, 51]. In addition to conventional electrochemical, mathematical, and equivalent circuit modeling, nowadays machine learning techniques even enable data-driven modeling for battery health and cycle life analysis [52, 53].

Despite the many proposed models found in the literature, one of the best-known mathematical models is Peukert's law, published in the late nineteenth century. The Peukert equation describes the nonlinear characteristic between the discharge current and the service time of a battery as follows:

$$C_P = I^k \cdot t \tag{2.1}$$

where: C_P is the Peukert or nominal capacity (i.e., energy) of the battery discharged at 1 A, I is the discharge current, t is the battery runtime, and k is the Peukert

number. This exponential coefficient, which is generally slightly above 1, describes the variation in the energy performance of a given battery concerning that at $I = 1$ A; the larger the value of k, the greater the difference in the capacity of the battery at currents different from 1 A. Although this mathematical expression was originally proposed for lead-acid batteries, it is now useful for batteries of other chemistries, even for electrochemical double-layer capacitors after the original equation was extended for the case of very high discharge currents [54]. However, the more general application of this equation requires some precautions [55].

In the literature, there are some revised definitions of Peukert's law. For example, it is reformulated in [56] as follows:

$$C_{n1} = C_n \cdot \left(\frac{I_n}{I_{n1}} \right)^{k-1} \tag{2.2}$$

In (2.2), C_n is the nominal capacity of a battery discharged at nominal current I_n, as defined by the manufacturer, whereas C_{n1} is the capacity when the battery is discharged at current I_{n1}. Although the original name of the Peukert coefficient in [56] is different, it is always called k in this document, for the sake of clarity and consistency.

So far, only continuous currents have been considered for the application of the aforementioned equations to batteries working at a constant temperature. However, as the performance of batteries generally depends on temperature, this parameter is considered in [57], through a mathematical model that extends the original equation by including an additional term with a coefficient (i.e., an exponential factor) to describe the relationship between battery performance and temperature, as follows:

$$\Delta C = \gamma \cdot \left(\frac{I_t}{I_{ref}} \right)^{\alpha} \left(\frac{T_{ref}}{T_t} \right)^{\beta} \tag{2.3}$$

In (2.3), ΔC is the discharged capacity, γ is the reference or nominal capacity [Ah], I_t and T_t are the current and temperature at time t, respectively, whereas I_{ref} and T_{ref} are the reference values; α and β are the exponential coefficients.

The previous limitation in applying Peukert's original law is that the analysis of operating time refers to discharge currents that are constant in time. Instead, there is now a need to analyze the performance of batteries discharged with pulse currents

in most modern devices (e.g., wireless sensors) and systems (e.g., battery electric vehicles), where the current and duration of the pulses can vary depending on the application and use. For this reason, an adaptation of the Peukert equation to pulse currents is needed. Nonetheless, for a better understanding of the principle on which the generalization of Peukert's law is based, two main effects are described hereafter: the *rate capacity effect* and the *recovery effect*.

Rate capacity effect

The "rate capacity effect" describes the difference in a battery's total capacity when depleted at different discharge currents [50]. It is a nonlinear characteristic of electrochemical batteries [58]. Indeed, today some cells minimize the rate capacity effect to ensure greater reliability and stable performance regardless of discharge current, especially at low and medium currents. This improvement in the energy performance quality of batteries is significant, for example, for the range estimation of uncrewed aerial vehicles (UAVs) and electric ground vehicles [59].

Although this effect is usually shown in battery manufacturers' datasheets for constant discharge currents, this effect can also apply to pulse currents to some extent. In this case, the rate capacity effect may have different characteristics.

Recovery effect

The "recovery effect" or "relaxation effect" is the property of certain batteries to recover part of the discharged energy during the rest phases after a current pulse. [60–62]. This is a fundamental characteristic as most of today's smart sensors work at intermittent power, as in the case of Internet of Things (IoT) applications [63]. Although alkaline cells appear to be very sensitive to energy recovery [47], lithium-based cells can also have this property. For example, the authors in [64] report the recovery effect for rechargeable lithium-sulfur batteries in automotive applications.

The recovery effect mainly depends on the magnitude of the current pulse, recovery period, and depth of discharge [64, 65]. In general, the impact of this property on battery performance depends on the chemistry of the cell. For this reason, the choice of the best battery for various applications should also consider the analysis of possible energy recovery. In fact, the consequent additional capacity,

due to the recovered energy, may improve the battery service time. For example, in the case of wireless sensors where data are collected and then transmitted at certain time intervals [66–68], or in electric vehicles where the discharge time of battery energy is followed by long rest periods [69].

In the literature, battery models including recovery effect analysis are uncommon. Only a few models have included this characteristic. For example, a stochastic model, in which the battery behavior is based on a Markov process, is proposed in [70], whereas an equivalent circuit model including the recovery effect is proposed in [71].

Generally, the difference in the energy performance of a battery discharged at various continuous currents primarily highlights the *rate capacity effect*. On the other hand, the comparison of the energy performance of the battery discharged at pulse currents with that at continuous currents makes the evaluation of the *recovery effect* possible.

2.1.2 Analysis of the recovered energy from datasheets

First, to adapt Peukert's analytical model to pulsed currents, it is necessary to quantify the energy recovered in the batteries during this discharge mode. The method described here to analyze directly from manufacturer's data is simply based on the following steps:

1. Extraction of the total capacity of a battery discharged at various pulse currents but similar long rest periods.
2. Extraction of the total capacity of a battery discharged at the continuous currents of the same magnitude as the pulse currents analyzed previously.
3. Computing the difference in battery capacity between pulse and continuous currents.
4. Finding the proper function of the additional capacity of the battery when discharged at pulse currents.

As an example, for the Energizer E91 alkaline cells (zinc-manganese dioxide, Zn/MnO_2), it is possible to extract the total service time from the datasheet [72] for the following pulse currents: 50, 100, and 250 mA, as reported in Table 2.1,

in which the last column reports the pulse "on" time and the rest time after each current pulse. Indeed, from the datasheet, it is possible to extract the capacity for a pulsed current of 750 mA. Since battery performance generally varies greatly when considering medium-high current rates, this current is not included here to prevent it from affecting other results inconsistently.

Table 2.1 Total capacity of the Energizer E91 cell, as extracted from the datasheet for various continuous and pulse currents.

Current [mA]	Capacity [mAh]		Note
	@ continuous	@ pulsed	
50	2816	2856	1 hour ON / 7 hours OFF
100	2600	2712	1 hour ON / 23 hours OFF
250	1900	2450	1 hour ON / 23 hours OFF

The resulting plot of the additional capacity of this battery, when discharged at pulse current instead of continuous current, is shown in Fig. 2.1.

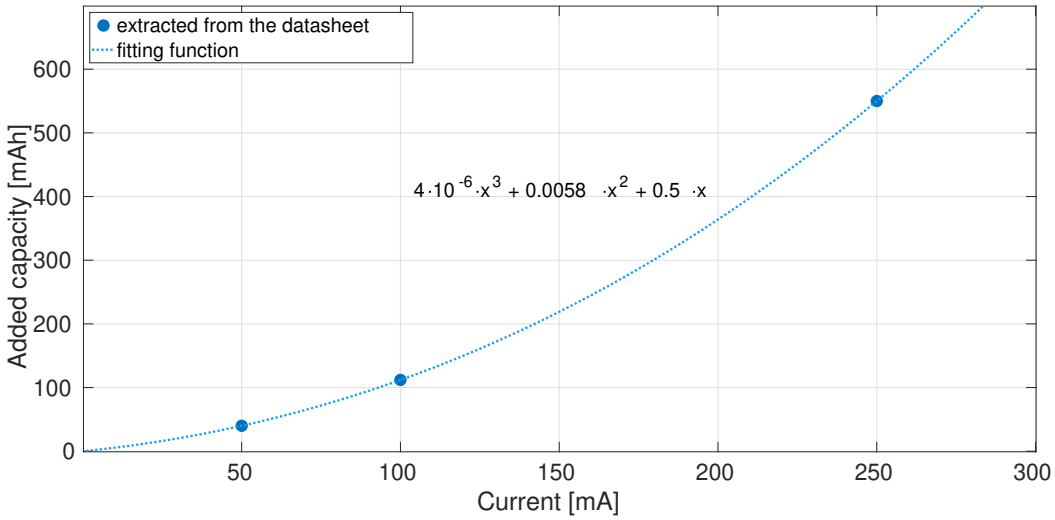

Fig. 2.1 Additional capacity when depleting the E91 battery by pulse currents instead of continuous currents.

The analytical expression of the fitting function is given in (2.4); it refers to the additional capacity for very long rest times only. It is assumed that the shorter the rest time, the less the recovered energy will generally be. However, this characteristic is expected to be different for high current rates, so the gain margin in using pulsed currents instead of continuous currents will no longer exactly follow this function.

$$C_{add} = 4 \cdot 10^{-06} \cdot {I_p}^3 + 0.0058 \cdot {I_p}^2 + 0.5 \cdot I_p \tag{2.4}$$

Generally, the recovery of the maximum recoverable energy between two consecutive pulses depends primarily on the battery chemistry and rest time. So, the shorter the pause time between pulses, the less energy will be recovered, even though not linearly. For this reason, the original Peukert equation cannot be directly applied to pulse currents. Or in other terms, this mathematical model needs to be adapted to the phenomenon of the recovery effect when this is present in batteries.

2.1.3 Generalization of the Peukert model

For batteries discharged at pulse rather than continuous currents, a new reference capacity and exponential factor must be defined to generalize Peukert's law. Therefore, the original equation reported in (2.1) is revised and adapted for the analysis of battery service time as follows:

$$t_{s_x} = \frac{C_{ref_x}}{{I_x}^{k_x}} \tag{2.5}$$

In (2.5), x is a generic subscript that stands for c or p, depending on whether the discharge current is continuous or pulsed, respectively, whereas t_s is net service time, which considers the battery runtime and, in the case of intermittent discharging, not the rest time. To extend the application of the Peukert model, the original C_p is changed to C_{ref}, as the reference capacity can be different from the Peukert capacity, depending on the battery use. Furthermore, although the reference current in the original Peukert equation is always 1 A, many battery cells have a different reference current, as for the case of wireless sensors operating in the order of milli- or submilliampere. In this case, both the reference capacity and battery current should be normalized to the reference current I_{ref}, regardless of the discharge mode, and the adapted Peukert model is therefore defined as follows:

$$t_{s_x} = \frac{C_{ref_x}}{I_{ref}} \cdot \left(\frac{I_x}{I_{ref}} \right)^{-k_x} \tag{2.6}$$

To find the parameter values leading to the best model accuracy, an algorithm is proposed hereafter.

Model parameters

For a given battery, after collecting some values of the total capacity for various currents in the same discharge mode, as obtained from the manufacturer's data or direct measurements, it is possible to extract the values of C_{ref_x} and k_x in (2.5), or (2.6) in the case of normalization, to characterize the battery performance in terms of maximum service time at different currents. The search algorithm implemented for determining the parameter values that minimize the model error for the actual data is described by Algorithm 1.

Algorithm 1 Search for the values of C_{ref_x} and k_x in (2.5)

1: $BestMaxErr \leftarrow \infty$.
2: **for all** $C_x = C_{nom}/2 \ldots C_{nom} \cdot 2$ **do**
3: **for all** $k = 1.000 \ldots 1.500$ **do**
4: $MaxErr \leftarrow 0$.
5: **for all** given $I_x \in [I_{min}, I_{max}]$ **do**
6: **if** $I_{ref} \; ! = 1\ A$ **then**
7: $C_x \leftarrow C_x / I_{ref}$
8: $I_x \leftarrow I_x / I_{ref}$
9: **end if**
10: Compute t_s by (2.5)
11: $\mathbf{Err}[I_x] \leftarrow Error\ (model\ vs.\ data)$
12: **end for**
13: $MaxErr \leftarrow argmax(\mathbf{Err})$
14: **if** $MaxErr < BestMaxErr$ **then**
15: $BestMaxErr \leftarrow MaxErr$
16: $C_{ref_x} \leftarrow C_x$
17: $k_x \leftarrow k$
18: **end if**
19: **end for**
20: **end for**

In the beginning, except for the initialization of the two variables for storing the errors (Lines 1 and 4), the algorithm defines two nested iterations for exploring the service time of the battery under test (Line 10) by applying (2.5) to each pair of the model parameters C_x and k (Lines 2–3). For such values, the service time is extracted for each given current I_x (Line 5). In the case of I_{ref} different from 1 A, C_x and I_x are then normalized (Lines 6–9) according to (2.6).

For each t_s, the model error is reported in the vector **Err** having the same number of elements of the given currents (Lines 10–11). If the maximum value ($MaxErr$) in **Err** is less than the best maximum error ($BestMaxErr$), then the latter is updated, and the values of C_x and k are saved (Lines 13–17).

Application example

The algorithm described above is then applied to the Energizer E91 battery. The model parameters are extracted when considering the continuous and pulsed discharge currents shown in Table 2.2, which reports the capacity and service time as extracted from the product data. The E91 battery is usually considered for consumer electronics where the load current is generally between 25 and 750 mA; in this case, I_{ref} is set to 100 mA.

Table 2.2 Total capacity and service time extracted from the Energizer E91 battery datasheet.

Current [mA]	Capacity [mAh]		Service time [h]	
	@ continuous	@ pulsed	@ continuous	@ pulsed
25	3045	-	121.80	-
50	-	2858	-	57.16
100	2534	2713	25.34	27.13
250	1991	2471	7.96	9.88
500	1520	-	3.04	-
750	-	2253	-	3.00

It is important to emphasize that, in intermittent discharge applications, the rest interval between current pulses is of the order of hours. This condition makes it possible to consider the maximum energy recovery during each rest interval. It should be noted that the list of the currents, for which the datasheet provides some information, is different when considering constant and pulse currents. The document reports the total capacity in the case of continuous currents and the service time (i.e., from full charge to cut-off voltage) in the applications of pulse currents. Nonetheless, in the latter case, the value of the total capacity for a given current can be obtained directly from $C = I_p \cdot t_s$.

The values of the model parameters obtained from the algorithm, which was implemented in Python (see Appendix A), are the following: C_{ref_c} and k_c are 2359 mAh and 1.232. respectively, for continuous currents, whereas C_{ref_p} and k_p are 2698 mAh and 1.090, respectively, for pulse currents. The maximum error of such models, after comparing the results with the manufacturer's data, is 6.9% and 0.55%, respectively. This first result confirms that Peukert's law can also be considered for batteries discharged with pulse currents by generalizing and adapting the original equation as previously described. Figure 2.2 shows the service time of the E91 battery for both discharge modes, as extracted from the datasheet and defined by the model.

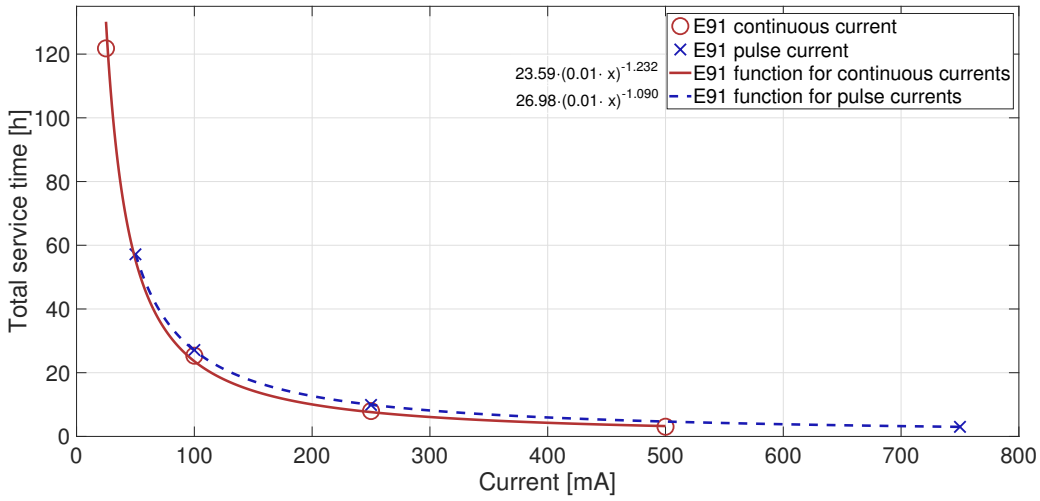

Fig. 2.2 Total service time of the E91 battery: model functions vs. datasheet. © 2022 IEEE

2.1.4 Results

As a further validation of the adapted Peukert model and the proposed parameter extraction method, an application to the Energizer L91 lithium battery (lithium/iron disulfide, Li/FeS_2) [73] is considered. In addition, some laboratory experiments have been carried out as a preliminary step to compare the results obtained with those of the manufacturer's data.

Laboratory Measurements

In six different experimental groups, fresh Energizer L91 batteries were discharged at three currents: 100 mA, 250 mA, and 750 mA, respectively. Three groups concern continuous currents, whereas three groups concern pulse currents. In the latter, each battery was discharged at the same capacity of 333.3 mAh during each pulse until the cut-off voltage of 0.8 V was reached. The rest period between two consecutive pulses was always 7 hours to ensure the greatest possible energy recovery. In addition, all the experiments were performed at room temperature. In any case, the performance of this battery is not affected by temperatures in the range of about 15 to about 25 °C [74].

The laboratory equipment includes a RIGOL DL3021 electronic load to discharge the batteries under test and an HP 34401A digital multimeter to measure the battery voltage. Table 2.3 reports the total service time of the twelve batteries tested.

Table 2.3 Experimental data for the Energizer L91 battery. © 2022 IEEE

Discharge current [mA]	Total service time [h]	
	@ continuous	@ pulsed
100	33.82	34.03
	34.24	34.11
250	13.27	13.36
	13.59	13.54
750	4.33	4.41
	4.46	4.46

For immediate understanding and analysis, Fig. 2.3 plots of the data obtained from direct measurements. It is worth noting that the performance of this battery is mostly constant when discharged with a continuous or pulsed current of the same magnitude. This characteristic is significant when considering this type of cell for various load applications. Furthermore, the total capacity obtained at a pulsed current is always within the range of the capacity obtained at a constant current of the same magnitude. One possible explanation for this result is that the temperature of a battery tends to be more constant when testing a pulse current. At the same time, it varies more with constant currents, leading to greater results differences due to

process and performance variations. Consequently, the higher the discharge current, the greater the uncertainty in the battery's total capacity.

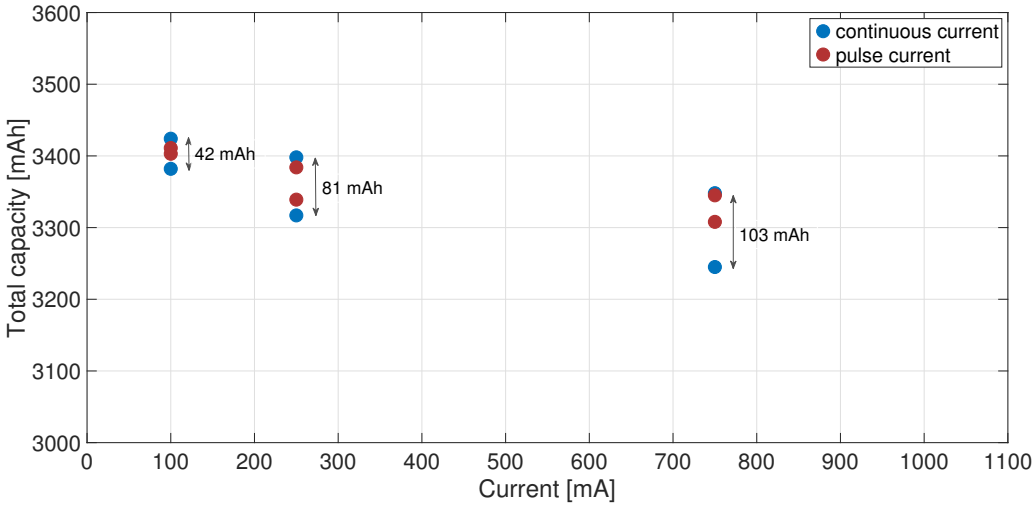

Fig. 2.3 Total capacity of the L91 battery as obtained from direct measurements.

The most important feature that can be deduced from the data is the largely stable performance of the L91 battery when discharged with a continuous current or a pulse current of the same magnitude at small and medium currents (up to 750 mA). In fact, after applying the methodology described in 2.1.3 to the mean values of the experimental data, for each current type and magnitude, the parameter values for the adapted Peukert equation are very similar, as given in Table 2.4. In this case, the maximum absolute errors of the model are truly negligible.

Table 2.4 Parameter values of the adapted Peukert equation for the Energizer L91 batteries under test. © 2022 IEEE

Current (mA)	@ continuous		Error	@ pulsed		Error
	C_{ref_c}	k_c	(%)	C_{ref_p}	k_p	(%)
100 ÷ 750	3405	1.016	0.1	3404	1.012	0.1

Manufacturer's Data

As a further validation and for a comparative analysis with the experimentally obtained results, the model parameters are also extracted from the manufacturer's data.

First, the total capacity of the L91 battery for various discharge currents is taken from the datasheet and the application manual [73, 74]. Figure 2.4 shows the results. They are grouped in pairs by current magnitude to provide an initial comparison of the battery's energy performance with respect to the discharge mode. The application

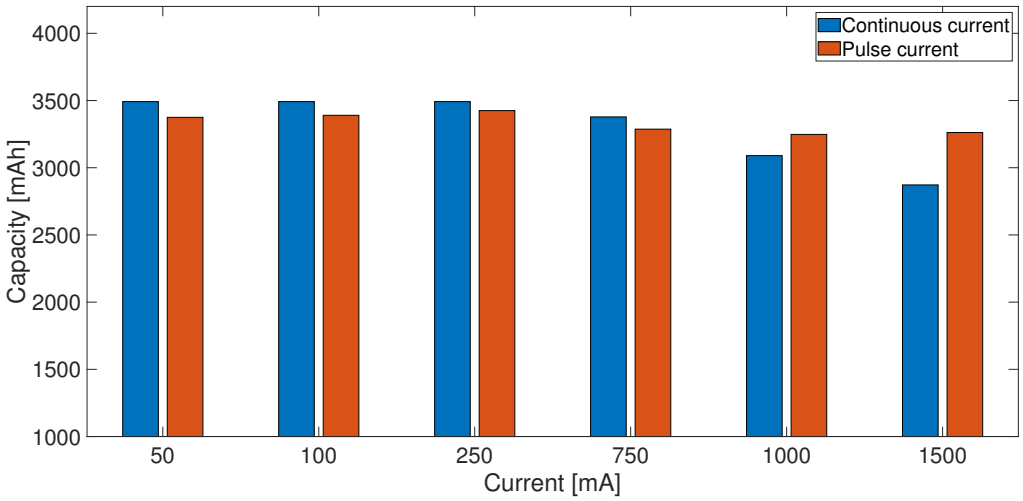

Fig. 2.4 Total capacity of the L91 battery as extracted from the manufacturer's data. © 2022 IEEE

tests with the pulse currents of 50, 100, and 250 mA include a cycle of one hour of discharge followed by a rest period of at least seven hours. In contrast, the industry standard test at 750 mA pulse current involves a discharge cycle of two minutes per hour and eight hours per day. Therefore, this application guarantees an energy recovery sufficient for a proper comparison with the other data since the rest time is always very long compared to the pulse time (i.e., a very small duty cycle). Also, the battery is not in use most of the day.

The first observation that emerges from the analysis of Fig. 2.4 is that, unlike the E91 battery, the total capacity of the L91 battery discharged with pulse currents is not greater than that obtained at low and medium continuous currents, as generally confirmed by the experimental data previously reported. In fact, for this battery,

the recovery effect is only evident at high currents (i.e., 1000 and 1500 mA). This leads to a second observation: the L91 battery shows two different behaviors when considering low and high discharge currents, respectively. This is shown in Fig.2.5, where the total capacity at low currents (i.e., from 50 to 250 mA) is shown in the upper graph and at high currents (i.e., from 750 to 1500 mA) in the lower graph. It is worth noting that the total capacity decreases sharply at high continuous currents, whereas it is not overly affected by pulse currents.

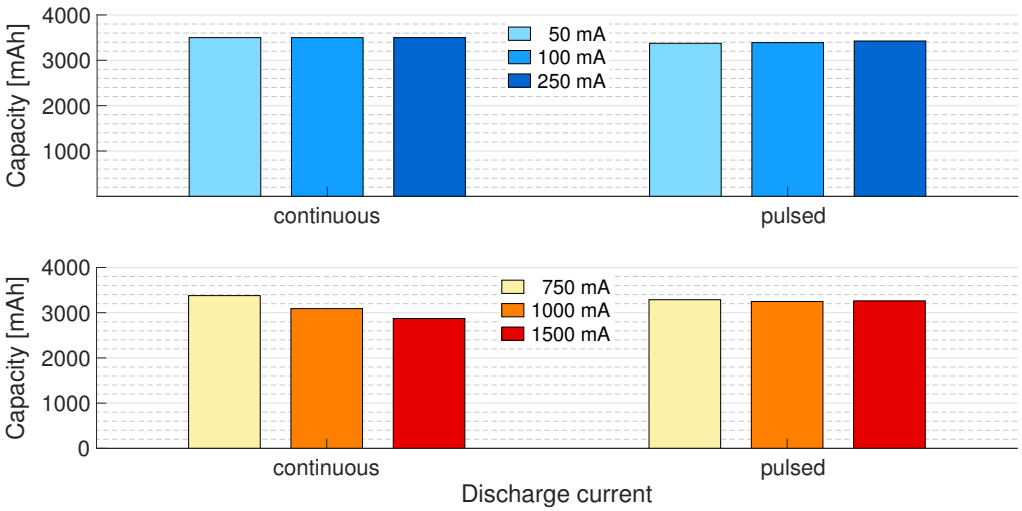

Fig. 2.5 A comparison of the total capacity of the L91 battery, as extracted from the product data, for low and high currents.

The adapted Peukert model is then applied to each of these two groups of discharge currents, with the 750 mA current also included in the low and medium current group, to ensure the continuity of this functional analysis of battery performance. Table 2.5 reports the parameter values of the model for this application. It is worth noting that C_{ref_c} is greater than C_{ref_p} at low and medium currents, while it is the opposite at high currents. Moreover, C_{ref_c} is very close to the nominal capacity of the L91 battery, namely 3500 mAh [73]. On the other hand, the values of the coefficients k_c and k_p are very similar and close to 1, except for the case of high continuous currents. They are also very close to the values obtained from the measurements: k_c and k_p are 1.012 and 1.010, respectively, as extracted from the datasheet for low and medium currents, while in the model obtained from direct measurements, they are 1.016 and 1.012 (see Table 2.4).

Table 2.5 Parameter values of the adapted Peukert equation for the Energizer L91 battery.

Current (mA)	@ continuous		Error	@ pulsed		Error
	C_{ref_c}	k_c	(%)	C_{ref_p}	k_p	(%)
50 ÷ 750	3496	1.012	1.0	3403	1.010	1.5
750 ÷ 1500	3123	1.233	1.1	3262	1.010	0.4

In addition, the original Peukert's law is applied to (i) the entire range of current values (i.e., from 50 to 1500 mA) and (ii) medium and high currents only (i.e., from 750 to 1500 mA). For this purpose, the original Peukert capacity C_P must be extracted from the application manual published by the manufacturer [74]. It is 3090 mAh in the case of a continuous current of 1 A. Moreover, the original Peukert equation is exceptionally applied to pulse currents to allow a thorough analysis. In this case, the total capacity extracted from the same manual is 3248 mAh. Table 2.6 reports the results, including the Peukert number for both applications and the model's relative maximum absolute percent errors with respect to the product data. It is worth noting that the accuracy of the original Peukert model degrades when the full range of currents is considered. This result confirms the chosen approach of considering the adapted analytical model separately for the two ranges of discharge currents.

Table 2.6 Parameter values of the original Peukert equation for the Energizer L91 battery.

Current (mA)	@ continuous		Error	@ pulsed		Error
	C_P	k	(%)	C_P	k	(%)
50 ÷ 1500	3090	1.063	6.9	3248	1.021	2.5
750 ÷ 1500	3090	1.233	2.1	3248	1.010	0.9

In Table 2.5 and Table 2.6, it can be seen that the exponential coefficient is the same at high currents and in both discharge modes (i.e., 1.233 and 1.010). Nevertheless, the error is always smaller in the case of the adapted model.

Discussion

First of all, there is remarkable stability in the energy performance of the battery, especially at small and medium current levels and at both continuous and pulse currents. This stability is also observed during pulsed discharge with medium-high currents, which only partially affect the energy performance. Instead, there is a gradual decrease in the total usable capacity of the battery when discharging with medium-high continuous currents. One of the reasons for this inconvenience is that high continuous currents lead to greater stress on the battery, for example, in terms of temperature.

Figure 2.6 contains two plots showing the service time of the L91 battery when discharged at low and medium currents (upper plot) and at high currents (lower plot). The values of model parameters C_{ref_c}, k_c, C_{ref_p} and k_p are given in Table 2.5. It is worth noting that C_{ref_c} is greater than C_{ref_p} at low and medium currents, while it is lower at high currents. On the other hand, the exponential coefficient k_c is very close to k_p (1.012 and 1.010, respectively) at low and medium currents, while it is very different (i.e., 1.233) at high currents. Conversely, k_p is 1.010 in both model functions; this confirms the stability of the energy performance of the L91 battery at pulse currents.

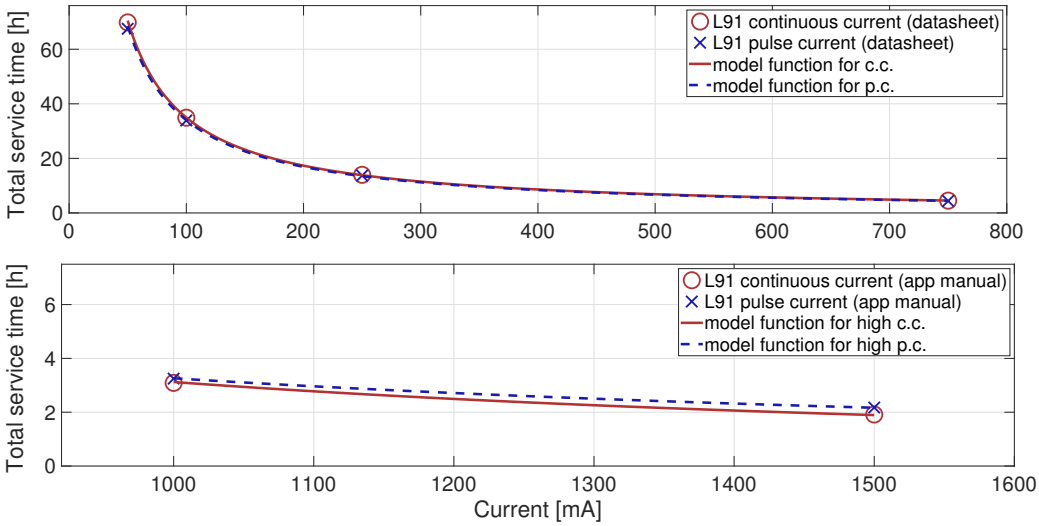

Fig. 2.6 Total service time of the L91 battery: model functions vs. datasheet. © 2022 IEEE

The application manual for the L91 battery specifies a duty cycle of 10% for high pulse currents [74]. Although this differs from the datasheet, which includes only

some applications at pulse currents from 50 to 750 mA, it is possible to include all the manufacturer's data in this work because they refer to pulse currents with a very low duty cycle. As a result, the applications considered may guarantee the maximum recoverable energy after each current pulse, and thus a condition opposite to that of continuous current from an energy point of view.

On the other hand, the model function that best describes the battery behavior requires the definition of two parameters and not only the exponential coefficient, as in the original Peukert model. This modeling approach leads to a higher accuracy than the one obtained by always considering the same reference capacity at the same reference current, as in the case of Peukert's law. In fact, the error of the proposed adapted model for the L91 battery is always less than 2%.

2.2 Comparison of batteries in IoT applications

2.2.1 Background and related work

The proliferation of battery-powered sensors and wireless device applications has led to the development of techniques and algorithms to reduce the energy consumption of conventional batteries and energy harvesters [75, 76]. Moreover, the interconnection of such devices in IoT networks requires an even more dedicated approach to the technical and economic analysis of these applications, where the reduction and control of energy costs have become key requirements. As a result, publications on battery cost models have also increased in the literature [77]. These models generally vary from material and manufacturing costs to performance and warranty costs [78].

Today, a comparison of the performance of different batteries is a standard measure in the development of new battery-powered devices and systems. This comparison is often based simply on analysis of rated capacity and battery life, the latter indirectly influencing device life and vice versa [79]. The total energy and aging of a battery usually vary under different working and operating conditions (i.e., load currents and temperatures). Therefore, a comprehensive investigation of battery performance is required, whether based only on manufacturer's claims or direct experimental data. To reduce this time-consuming activity, such a comparison is often limited to a few working and operating conditions or the analysis of a

summary table containing only the most essential characteristics of the batteries under consideration [80].

In the case of battery-powered devices, several works aim to extend the life of batteries to reduce the number of replacements and the associated costs. In this context, batteries for low-power sensing and IoT devices are mainly primary batteries due to their low cost and self-discharge. This is the case, for example, of IoT devices with multiple sensors to monitor energy efficiency in buildings or damage to civil structures [81, 82].

In general, alkaline and lithium-ion (Li-ion) batteries are preferred to other batteries with different chemistry because they have high energy density (kWh/kg) and do not require maintenance [83]. However, these batteries differ in their characteristics and, consequently, in their cost. In addition, lithium is widely available on Earth [84]. For this reason, they are currently preferred for most modern devices and systems, although current research studies are focusing on batteries based on new chemistries [85].

The method for selecting the best battery varies greatly depending on the application. For example, the selection of cells for the construction of battery packs requires a very extensive preliminary analysis ranging from the mechanical (e.g., pressure) to the thermal performance of such cells. In this context, some tools have been developed, such as *BaTPac*, developed by Argonne National Laboratory for the complete analysis of battery manufacturing costs, especially for the automotive industry [78], and the cost-benefit analysis tool proposed by Hitachi for the application of battery storage systems in electric power grids [86]. However, these tools are usually designed for large battery packs and are, therefore, too complex for battery cell selection for IoT applications. For this reason, this work proposes a more straightforward and intuitive cost model for selecting batteries from the perspective of their purchase price versus their performance, although the analysis for selecting batteries in IoT sensors from a cost-benefit perspective is indeed non-trivial, since battery performance generally does not have linear characteristics. This section describes a workload-based methodology and cost model for comparing primary batteries of different chemistries. This study explains how the nonlinear characteristics of different batteries can be comprehensively analyzed from the user's perspective to select the most suitable battery for a given application from an economic point of view.

2.2.2 Cost model

For a given set of battery-powered sensors, the replacement of the batteries is usually not synchronized because these batteries do not usually reach their end of life (EOL) simultaneously. For this reason, the total cost of battery replacement for a given set of IoT devices over a given period is defined as follows:

$$c_{tot} = \sum_{i=1}^{n} (N_{b_i} \cdot c_{b_i} + c_{r_i}) \tag{2.7}$$

where c_{tot} is the total cost of the battery after n replacements of the discharged batteries, and for each ith replacement:

N_b is the total number of replaced batteries in the devices,

c_b is the cost of one battery,

c_r is the labor-related replacement cost.

For a comparison of two batteries, B_H and B_L, with the former having a capital cost c_{B_H} higher than the capital cost c_{B_L} of the other battery, the cost index (J) is defined as the ratio c_{B_H}/c_{B_L}. In this context, the capital cost is the purchase price.

On the other hand, the break-even cost index (J^{ε}) based on the performances of such batteries is defined as follows:

$$J^{\varepsilon}(t_s) = \frac{t_{s_{B_H}}}{t_{s_{B_L}}} \tag{2.8}$$

where $t_{s_{B_H}}$ and $t_{s_{B_L}}$ indicate the service time of B_H and B_L at a given current and discharge mode (i.e., continuous or pulsed), as computed by (2.6). As the service time generally differs for batteries discharged at various continuous and pulse currents, J^{ε} is commonly a non-linear function; this will be demonstrated in Section 2.2.3.

Now one can compare J with J^{ε} to evaluate whether the ratio of the purchase prices of B_H and B_L can be justified by the better performance of B_H over that of B_L. However, to extract the value of J^{ε} for the operating point of the batteries, it is always necessary to consider a specific application. In practice, J^{ε} shows the actual cost ratio of B_H compared to B_L when evaluating the performance of these batteries. For example, if the purchase price of B_H is twice that of B_L, the performance of B_H should be at least twice as high for a given application. However, the comparison

between J and J^{ε} does not take into account the labor-related replacement cost c_r. For this reason, the total break-even cost index, including c_r is defined as follows:

$$J^{\varepsilon}_{tot} = J^{\varepsilon} + \frac{c_r}{c_{B_L}} \cdot (J^{\varepsilon} - 1), \qquad J^{\varepsilon} \geq 1 \tag{2.9}$$

In (2.9), c_r is normalized to the cost of B_L, and the relationship between J^{ε} and C_r is linear. For example, $J^{\varepsilon} = 2$ means that exactly two batteries B_L are needed to achieve the same service time as one battery B_H. This means that the first B_L, when exhausted, must be replaced by a new one to achieve the same service time as B_H. Finally, both the second B_L and the original B_H are replaced at the same time (the net replacement time of the battery is neglected here).

For rechargeable batteries, the replacement cost is generally replaced by the charging cost, except for the case of EOL. For this reason, the difference in capacity fading (i.e., the irreversible capacity loss) of two different secondary batteries should always be considered to provide a valid comparison of their performances. Also, maintenance costs should be considered for large-scale storage systems or energy harvesters. The latter sometimes used with electrochemical batteries for wireless devices [75].

2.2.3 Results

As an application example, the comparison in the performance of the Energizer E91 alkaline cell (zinc-manganese dioxide, Zn/MnO_2) [72] and the Energizer L91 lithium cells (lithium/iron disulfide, Li/FeS_2) [73] is made through the proposed cost model. Although cylindrical primary batteries are involved, the method can be applied to other types of batteries (e.g., button cells), even rechargeable batteries, but with some precautions, as mentioned before.

This section first describes the battery performance analysis based only on battery datasheets. Then, direct experimental data are given for validation. Finally, another point of analysis is reported on the performance of the batteries at various operating temperatures.

Manufacturer's data

Often, the preliminary selection of batteries for IoT sensors is based on information provided by manufacturers rather than direct laboratory experiments, which usually take a lot of time. For this reason, an initial analysis is performed here using only the manufacturer's published product data for the E91 and L91 batteries [72, 73]. Although data for only a few discharge currents were mainly published in the datasheets, the power functions of these batteries can be extracted using the adapted Peukert model defined in (2.6), where I_{ref} is 100 mA for both battery types. Table 2.7 gives the parameter values of the models for continuous and pulse discharge currents, respectively, and the nominal capacity specified by the manufacturer.

Table 2.7 Parameter values of the adapted Peukert equation for the Energizer E91 and L91 batteries discharged at low and medium currents.

Battery	C_{nom} [mAh]	@ continuous		@ pulsed	
	@100 mA	C_{ref_c}	k_c	C_{ref_p}	k_p
E91	2500	2359	1.232	2698	1.090
L91	3500	3496	1.012	3403	1.010

For a visual analysis of such performance-related functions, Fig. 2.7 and Fig. 2.8 report the plots of the original data and the model functions regarding the service time of the E91 and L91 batteries discharged with continuous and pulsed currents, respectively.

The maximum error of the models to the product data is always less than 2.0%, except for the continuous current discharge model of the E91 battery, where the maximum error is 6.9%. When comparing different batteries, the range of values in which the characteristics are available also differs from one datasheet to another. For example, the E91 battery datasheet gives the total capacity, from which the total service time can be derived only up to a continuous current of 500 mA. On the other hand, the total capacity of the L91 battery is also given for higher currents in the datasheet.

Figure 2.9 shows the break-even cost index, as defined in (2.8) and referred to here as time index, of the L91 battery compared to the E91 battery. For example, it can be seen, that the operating time of the L91 at a continuous current of 400 mA is

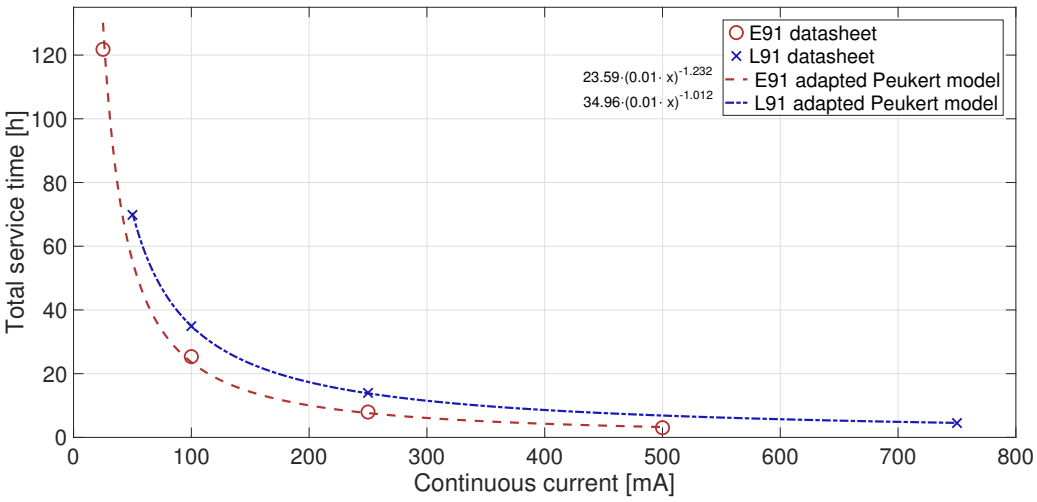

Fig. 2.7 Total service time of the E91 and L91 batteries at continuous currents.

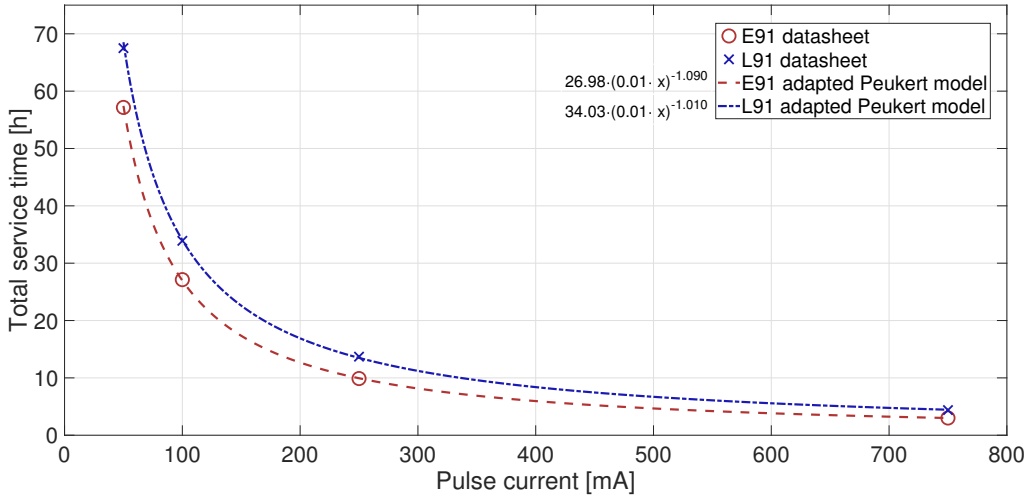

Fig. 2.8 Total service time of the E91 and L91 batteries at pulse currents.

slightly more than twice that of the E91 (i.e., $J^{\varepsilon} \approx 2$), while at 50 mA it is only 30% higher (i.e., $J^{\varepsilon} \approx 1.3$).

Because the manufacturer's specifications for battery capacity or service time apply to battery currents from 50 to 500 mA for both batteries and each discharge mode (i.e., continuous and pulsed), Fig. 2.9 reports J^{ε} in the same range.

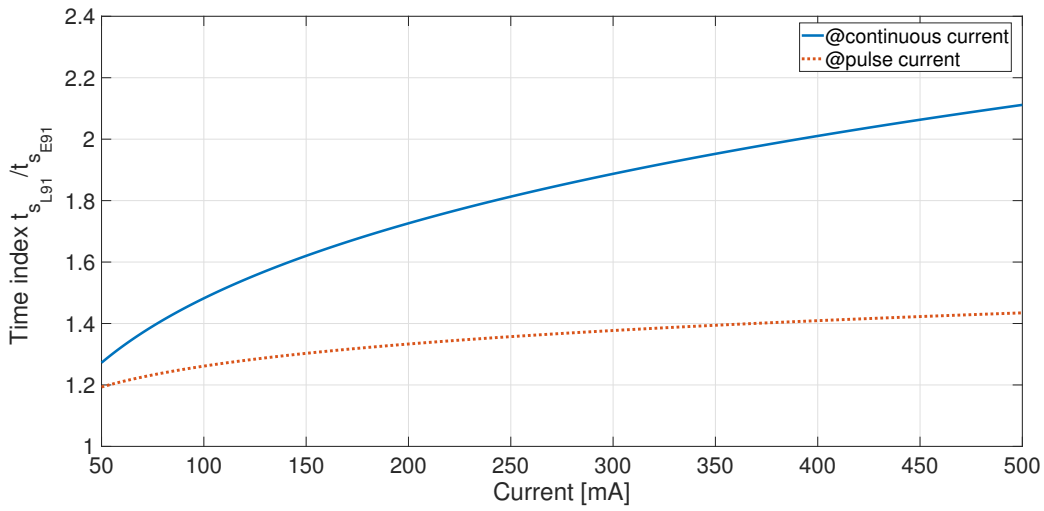

Fig. 2.9 Time index of the L91 battery vs. E91 battery for continuous and pulse currents.

Experimental data

For validation, various experiments were performed on discharging Energizer E91 and L91 batteries at 100 mA and 250 mA. The laboratory instruments consisted mainly of one RIGOL DL3021 programmable electronic load and one HP 34401A digital multimeter. In the case of pulse discharge, the rest time between two consecutive pulses was at least 1 hour, and in some experiments, several hours to ensure possible energy recovery in the tested batteries. This approach is consistent with the datasheets that give standard tests with similar rest periods. In addition, all experiments were conducted at room temperature, as were the tests specified by the manufacturer. Minor differences in room temperature around 20°C should not affect the performance of the batteries considered here, especially the L91 battery, as indicated in the handbook and application manual [74]. Table 2.8 reports the total service time obtained during the experiments. Since different batteries were tested under the same working conditions, the mean value of the service time is given here.

Figure 2.10 shows a comparison of the experimental data with the manufacturer's data. The total capacity of the batteries is almost the same in most cases, except for the discharge state of the E91 battery at a current of 250 mA, whether continuous or pulsed. In this case, the difference is about 15%. This difference is expected for alkaline batteries, as they generally have less stable performance than lithium batteries. In all other scenarios, the difference is limited, and this may be due to

Table 2.8 Experimental data of the tested Energizer E91 and L91 batteries.

Current [mA]	Service time [h]			
	E91		L91	
	@ continuous	@ pulsed	@ continuous	@ pulsed
100	25.31	27.37	34.03	34.07
250	6.77	8.23	13.43	13.45

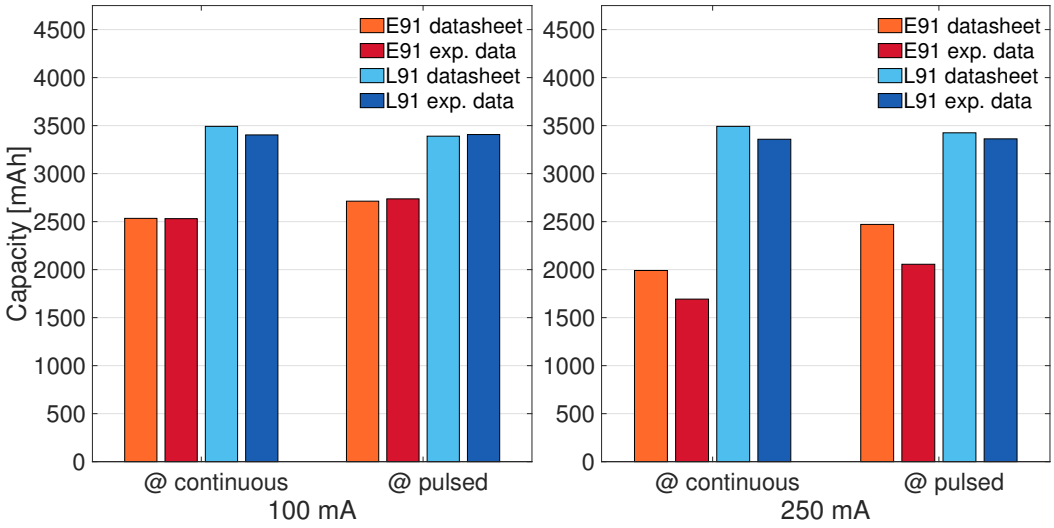

Fig. 2.10 A comparison of the total capacity obtained from the experimental results with the manufacturer's data for the E91 and L91 batteries discharged at 100 and 250 mA.

several reasons, such as process variation during manufacturing and calendar aging due to the time the batteries were stored before being used for the experiments.

Temperature-dependent capacity

So far, the comparison has been based on the cost of batteries versus their performance service time at a reference temperature. However, for a comprehensive analysis, two other parameters must be considered: (i) the temperature effect on battery capacity and (ii) shelf life. For example, the datasheets of E91 and L91 batteries state their shelf life as 10 and 20 years, respectively. On the other hand, battery performance in terms of capacity as a function of operating temperature is

only sometimes specified in many battery datasheets, except in other documents published by manufacturers. For example, the handbook of the alkaline batteries [87], which includes the E91, reports that temperature greatly effects the total capacity of this battery, even in a non-linear way with respect to currents. For this reason, temperature cannot be neglected, as many IoT applications today are designed for outdoor use and thus for a wide operating temperature range. It should be noted, however, that the characteristics *C vs. T* given by the manufacturers generally only refer to continuous currents.

For a thorough cost-benefit analysis, the capacity index is defined as the ratio of L91 and E91 battery capacity, i.e., C_{L91}/C_{E91}, where both C_{L91} and C_{E91} are temperature-dependent functions for different currents. Figure 2.11 shows the capacity index for 25 mA, in the case of low-power applications, and 250 mA, which is a medium current for these batteries.

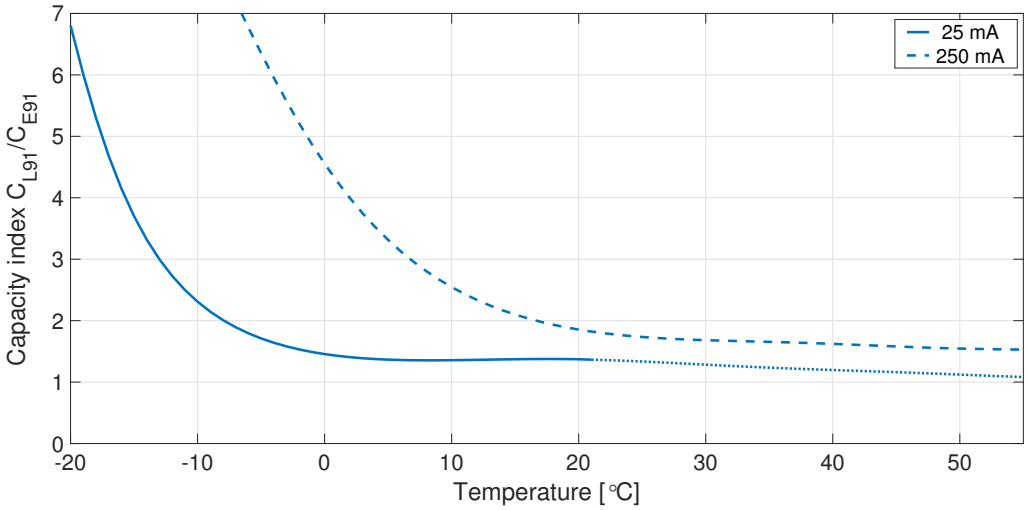

Fig. 2.11 Capacity index of the L91 battery vs. E91 battery as a function of temperature.

All these data were extracted from the application manuals of the batteries [74, 87] except for battery L91, which is discharged with a continuous current of 25 mA. In this case, the datasheet gives the total capacity only for temperatures lower than 21 °C. Nevertheless, it is possible to estimate this function for temperatures above 21 °C (see the dotted line in Fig. 2.11) using the data for the current of 50 mA, as given in the application manual. Indeed, the total capacity of the L91 at temperatures above 21 °C appears to be generally independent of the small and medium discharge currents, although slightly decreasing.

The most crucial information that can be gleaned from the plots in Fig. 2.11 is that the capacity of the E91 alkaline battery almost reaches the capacity of the L91 battery at high operating temperatures, at most 55 °C, and low discharge currents. This is because the total capacity of the L91 battery decreases slightly at operating temperatures above 21 °C, while the E91 battery increases its energy capacity rapidly at such temperatures. Conversely, this capacity decreases dramatically at temperatures below the reference temperature so that the capacity of the L91 is significantly greater than that of the E91, even several times at very cold temperatures.

Chapter 3

Energy Optimization for Electric Vehicles

Some of the work described in this chapter was also previously published in [88, 89]. Compared to [88], some sentences and paragraphs have been changed and adapted to this thesis other than (i) removing the graph related to battery price over the years and (ii) updating the original plot *battery energy vs. travel distance* for the plug-in hybrid electric vehicle under observation.

3.1 Battery cost in EVs

3.1.1 Introduction

The recent, remarkable increase in the production and utilization of electric vehicles (EVs) is decreasing the use of petroleum products, and gradually accomplishing the challenge of decarbonizing road transport to reach the goal of reducing CO_2 emissions [90]. For instance, the number of electric light-duty vehicles in the world, including full-battery electric vehicles (BEVs) and plug-in hybrid electric vehicles (PHEVs), practically tripled in a few years, so continuing an exponential trend during the last decade [91]. However, the fluctuations in EV sales are constantly evolving, even in terms of the EV type [92], depending on the geographic area considered. For example, in 2021 about half of the sales were in China, where BEVs are largely the majority, while electric car registrations and sales increased in the United States, but

after two years of decline. In Europe, where the number of BEVs and that of PHEVs are generally closer to each other when compared with those in the U.S. and China, the increase continues very remarkably [91]. Nevertheless, the transformation of the existing very large, global fleet of conventional internal combustion engine (ICE) vehicles will take several more years [93].

This notable increase in the EV market is one of the reasons for the rapidly decreasing price per kilowatt-hour of battery packs [94] and the significant increase in research and development for new batteries of various chemistries with ever-improving performance [85]. Nonetheless, the cost of batteries still weighs heavily on the total cost of electric cars, especially in the case of BEVs. In fact, car makers may take advantage of the lowered cost of battery cells to increase the total capacity of battery packs by adding a greater number of cells, in order to increase the maximum mileage or driving range of their BEVs before charging. This solution reduces the so-called range anxiety in EV drivers [95].

The analysis of the degradation in rechargeable (i.e., secondary) batteries generally considers the maximum number of equivalent cycles before reaching the state of health of a battery equal to 80%, that is, an irreversible loss of 20% of its nominal capacity [96]. However, part of this capacity fading is also due to irreversible degradation over time, also known as calendar aging, which should be investigated in applications where rest time far exceeds that of active operation, such as in the case of EVs [97, 98]. Therefore, the real cost of a car battery strictly depends on the time interval for a pack to reach its end of life and its consequent replacement with a fresh one [88].

The proposed cost analysis model includes the degradation trend of battery life over time for PHEVs and BEVs, in which the size and actual use of their batteries differ. As the stress and aging of these batteries also depend on mobility characteristics (i.e., urban, highway, etc.), the model is applied to various scenarios according to the Vehicle Chassis Dynamometer Driving Schedules defined by United States Environmental Protection Agency [99]. The cost model allows for the following:

- Analysis of the battery usage of BEV and PHEV depending on mobility characteristics
- Analysis of the optimal usage cost of batteries in order to maximize the benefit-cost ratio

- Analysis of the battery degradation based on battery usage, warranty and capacity.

3.1.2 Background and related work

Most EVs can be classified into two large groups: battery electric vehicles and hybrid electric vehicles, the latter still retaining the traditional internal combustion engine as the main power source. Both of these groups can be further divided into subgroups. The first group can be subdivided into full-battery (BEV) and range-extended battery (BEVx or REEV) electric vehicles, and the second group can be subdivided into full-hybrid (FHEV or HEV) , plug-in hybrid (PHEV) and mild-hybrid (MHEV) electric vehicles, as shown in Figure 3.1 (green-based and blue-based colors, respectively).

As reported in [92], the current global demand for BEVs, FHEVs and MHEVs is generally evenly split, while the demand for PHEVs is about half of that for BEVs or MHEVs. However, this distribution could easily change due to the impressive year-over-year growth in EV production and sales, making market share prediction more uncertain.

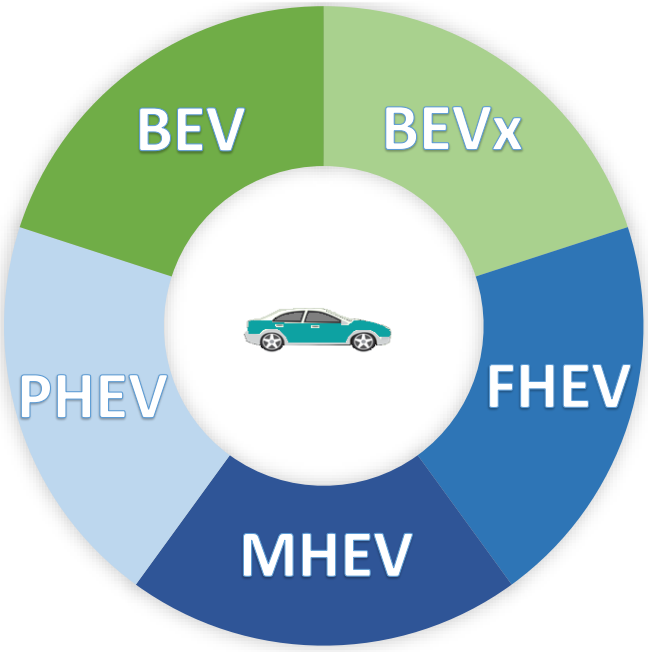

Fig. 3.1 The main electric and hybrid vehicle types in the market.

Indeed, a BEVx has a fuel auxiliary power unit (APU) to extend the maximum mileage. However, a BEVx is still considered a full-battery electric vehicle, as the use of the auxiliary unit is a fallback option to charge the battery when mostly depleted, and not a normal operating condition [100]. For this reason, the market share of this EV type is usually included with that of the BEVs. Although micro-hybrid electric vehicles are sometimes included among EVs, in this analysis they are not considered as they are basically traditional ICE vehicles with electric start-stop systems.

For light-duty vehicles, such as passenger cars, the energy size of the battery packs in EVs generally differs greatly depending on the type of vehicle: (i) usually less than one kilowatt-hour for MHEVs, (ii) up to about 20 kWh for FHEVs and PHEVs, and (iii) in general several tens of kilowatt-hours for BEVs, even up to or greater than 100 kWh [101]. However, the size of battery packs tends to increase with later-model EVs in order to achieve an ever-greater autonomy of distance that more closely approaches that of traditional vehicles. This impressive use of batteries in EVs, has also led to the search for ways to repurpose these batteries after their use in electric vehicles. This research activity has been ongoing during the last decade to reduce the total life cycle costs of these batteries [102]. Most battery packs consist of lithium-based cells due to their high specific energy [Wh/kg] and the large availability of lithium on the Earth [103].

The analysis of the performance, aging and cost of battery cells has captured the attention of both car manufacturers and researchers [94, 85, 77]. For example, many battery simulation models have been proposed in the literature, from electrochemical and mathematical models to equivalent electrical circuits [104]. They are populated by using direct experimental data and/or manufacturer's data. In the latter case, the model accuracy depends on the amount and quality of information reported in public datasheets [105]. However, these models are directly concerned with performance only. Conversely, cost models are obviously more concerned with the economic, rather than the technical aspects. An overall analysis of the costs related to battery wear is indeed very important from an owner's perspective.

At system level, the models of the capacity fade in batteries (i.e., the reduction of the maximum available energy) due to cycle life generally consider average state of charge (SOC), temperature, depth of discharge (DOD), and C-rate (i.e., battery current normalized to nominal capacity) [106–108]. Accurate models also include the analysis of calendar aging.

The Urban Dynamometer Driving Schedule (UDDS) is a test defined by the EPA for analyzing the performance, especially the CO_2 emissions of vehicles in urban mobility, which usually includes many start-and-stop phases [109]. In this context, the authors in [110] and [111] analyzed the energy performance of some BEVs and PHEVs in real-world driving, but they did not consider battery aging. Similarly, electrical energy and fuel consumption for these vehicle types were analyzed in [112], resulting in some interesting conclusions regarding the optimal size of the battery packs from an energy perspective, especially in the case of PHEVs.

An annualized total cost of ownership of electric passenger cars was analyzed in [113]. The proposed model also includes investment cost, maintenance cost, and insurance cost. However, battery cost is changing considerably in EVs during these recent years and, therefore, it truly affects the fluctuating cost of ownership. In general, the cost of depreciation of a battery pack over time is commonly included in maintenance costs [114].

3.1.3 Cost model

The basic equations of the proposed cost model for battery usage are defined hereafter. The minimal or optimal daily cost of battery usage is given by:

$$c_{d_{min}} = \frac{c_{tot}}{N_{d_{max}}}. \tag{3.1}$$

where c_{tot} is the total cost of a fresh battery pack and $N_{d_{max}}$ is the estimated maximum number of days of service. Then, the minimal cost of battery usage after N_d days of service is given by:

$$c_{min} = c_{d_{min}} \cdot N_d. \tag{3.2}$$

Then, the actual cost of battery use is defined as follows:

$$c_a = c_{tot} \cdot \frac{C_f}{C_{f_{max}}}. \tag{3.3}$$

where C_f and $C_{f_{max}}$ are the actual capacity fade and maximum capacity fade of a battery, respectively.

Battery usage index, or cost index, after N_d days of service is given by:

$$\alpha = \frac{c_a}{c_{min}}. \tag{3.4}$$

Therefore, this index has three main results:

$$\alpha = \begin{cases} < 1 & : battery\ is\ underused \\ = 1 & : battery\ is\ used\ optimally \\ > 1 & : battery\ is\ overused \end{cases}$$

Therefore, if $\alpha < 1$ then the replacement of the battery will take place as a consequence of the expiry of the warranty rather than the achievement of the maximum number of equivalent cycles, and vice versa in the case of $\alpha > 1$. Although this basic usage cost analysis is the same for all-electric vehicles, the total cost for the energy consumption in BEVs and PHEVs differs as reported below.

Battery Electric Vehicle

In BEVs, the energy cost is defined as follows:

$$c_{BEV} = \sum_{i=1}^{N_d} E_e(i) \cdot p_e(i) + c_a. \tag{3.5}$$

where E_e and p_e are the energy and unit price of electricity, respectively, for each day of use i.

Plug-In Hybrid Vehicle

PHEVs use two different energy sources: electricity and gasoline. Therefore, the degradation of battery life over time tends to differ from that in BEVs. Furthermore, the energy cost is also affected by fuel price as follows:

$$c_{PHEV} = \sum_{i=1}^{N_d} (E_e(i) \cdot p_e(i) + E_g(i) \cdot p_g(i)) + c_a. \tag{3.6}$$

where E_g and p_g are the energy (in this case, "amount") and unit price of gasoline, respectively, for each day of use i.

3.1.4 Simulation setup

There are several vehicle simulators, in both academia and industry, for the analysis of the energy consumption and/or gas emission of vehicles. Among them, the chosen tool is ADVISOR (ADvanced VehIcle SimulatOR), a MATLAB/Simulink based open-source simulator. It is widely used for research studies in academia because of several merits [115]. First, ADVISOR is free and supports various frameworks for ICE vehicles, PHEVs, and BEVs that are sold successfully in the market. Second, it also allows access to detailed simulation codes and vehicle simulator updates in an easy way. In this context, the simulation of the overall energy flow of EVs is carried out by considering the vehicle powertrain model, drivetrain model including power transmission system, and battery SOC estimator. ADVISOR includes detailed model coefficients of engines, electric traction motors, controllers, converters, energy storage systems, shapes of chassis, etc. The specification and efficiency of the components were scaled and tuned carefully in order to simulate the following vehicles: Tesla Model 3 and Toyota Prius Prime. These car models has been selected because they were the best-selling BEV and PHEV, respectively, in the United States in 2019 [116]. Furthermore, Model 3 is the first plug-in electric car to reach one million sales in June 2021 [117]. The specifications for these EVs are then reported hereafter.

1. BEV: The curb weight of Tesla Model 3 is 1611 kg, and the drag coefficient is 0.23 [118]. Model 3 is a rear-wheel-drive car and includes a maximum 211 kW AC permanent magnet motor and a 50-kWh lithium-ion battery pack.

2. PHEV: Toyota Prius Prime is based on the XW50 model (the fourth-generation Prius) [119]. It is a front-wheel-drive car, the curb weight is 1,526 kg, the drag coefficient is 0.24, and the powertrain is 1.8 L (1,798 cc) Atkinson cycle engine with an electric motor. The maximum power and torque of the motor are 53 kW and 163 Nm at 4000 RPM, respectively. This car includes an 8.8 kWh lithium-ion battery pack. It is assumed that it consists of lithium-ion cells of the same type used in Model 3, in order to coherently compare the battery

SOC and battery aging of the selected PHEV and BEV under the same battery characteristics.

Indeed, the degradation of the battery of a PHEV operating in charge-depleting mode is comparable to that of a BEV, as the traction energy is provided exclusively by the battery in both cases. Conversely, the degradation of the battery of a PHEV changes in the case of a traditional ICE also providing energy for the vehicle. For this reason, the comparison of battery costs here is based on the analysis of the selected BEV and PHEV in charge-depleting mode and hybrid mode, respectively.

3.1.5 Results

Analysis of Driving Simulation Results

Initially, the driving simulation test is carried out on a typical city driving condition with the Urban Dynamometer Driving Schedule (UDDS) defined by EPA and analyzed the operation and related energy consumption of the electric cars considered in this work. Figure 3.2 shows the simulation results for the BEV and PHEV under the UDDS cycle, whose overall driving time is about 22.8 minutes to drive 12 km, so that the average speed is 31.5 km/h during 17 stops and goes. The maximum speed is 91.2 km/h.

Figure 3.2(a) shows the power consumption by the electric motor of the BEV under test. All the power consumption is directly related to battery SOC. It is worth noting that the electric motor in the BEV regenerates electricity during deceleration through regenerative braking; this is identified by negative power in the figure. On the other hand, Figure 3.2(b) shows the power consumption by the engine and electric motor of the PHEV under the same driving profile. Most of the power for PHEV accelerations comes from the engine, whereas the electric motor only assists as a sidekick. Although energy recovery from regenerative braking is possible in PHEVs, the amount of such energy is generally less than that obtained in BEVs because of the smaller size of the motor.

Figure 3.3 enlarges the time period from 250 s to 500 s of the simulation test depicted in Fig. 3.2. Figure 3.3(a) refers to the speed profile. Figure 3.3(b) shows the power of the BEV motor and the battery SOC, which decreases when the power is positive (energy consumption) and increases when the power is negative (recovered

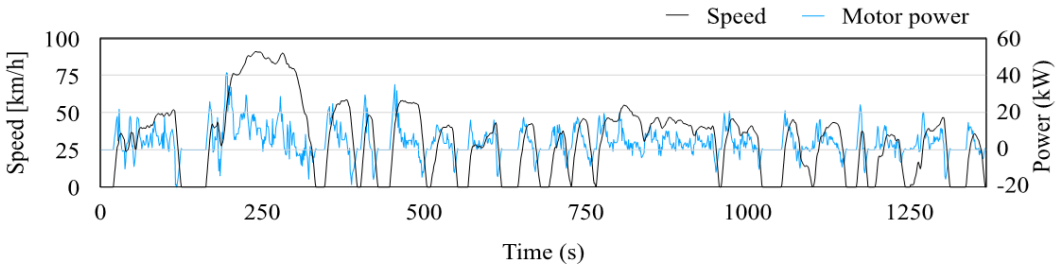

(a) BEV power consumption.

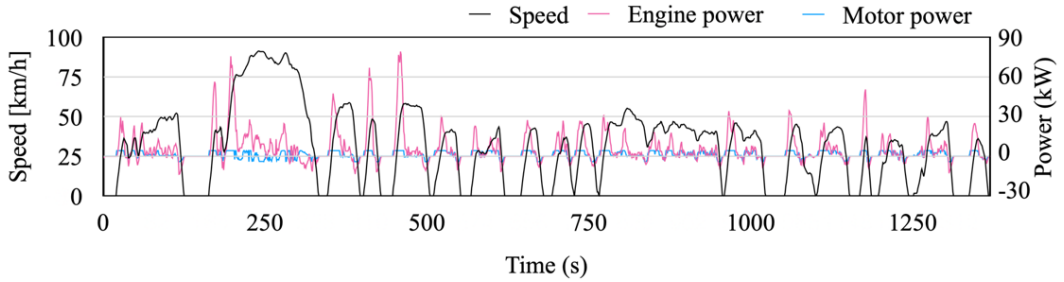

(b) PHEV power consumption.

Fig. 3.2 Simulation results of the UDDS test cycle.

energy) during regenerative breaking; these braking periods are highlighted in light blue color. Figure 3.3(c) shows the engine power, motor power and battery SOC of the PHEV. In this case, the battery is charged by (i) the electricity generation from the engine, and (ii) the electricity generation from the electric motor through regenerative braking. The charging periods are highlighted in magenta color and marked from 1 to 5. The first, third and fifth period (i.e., 1, 3 and 5) resulted from the electricity generation of the engine, whereas the second and fourth periods (i.e., 2 and 4) resulted from the regenerative braking.

Table 3.1 shows the overall energy consumption and related costs by electricity and gasoline for the BEV and PHEV under the UDDS driving test. In this analysis, the electricity price p_e is 0.375 $ per 1 kWh, whereas the gasoline price p_g is 1.472 $ per 1 kg [120, 121]. In general, PHEV owners spend much more money on gasoline than electricity. One of the reasons is that a part of the electrical energy is generated by the engine in addition to regenerative braking. On the other hand, BEV uses only the electrical energy, and part of this energy is recovered by regenerative braking with a relatively large motor. Therefore, the total energy cost for a PHEV is higher than the total energy cost for a BEV.

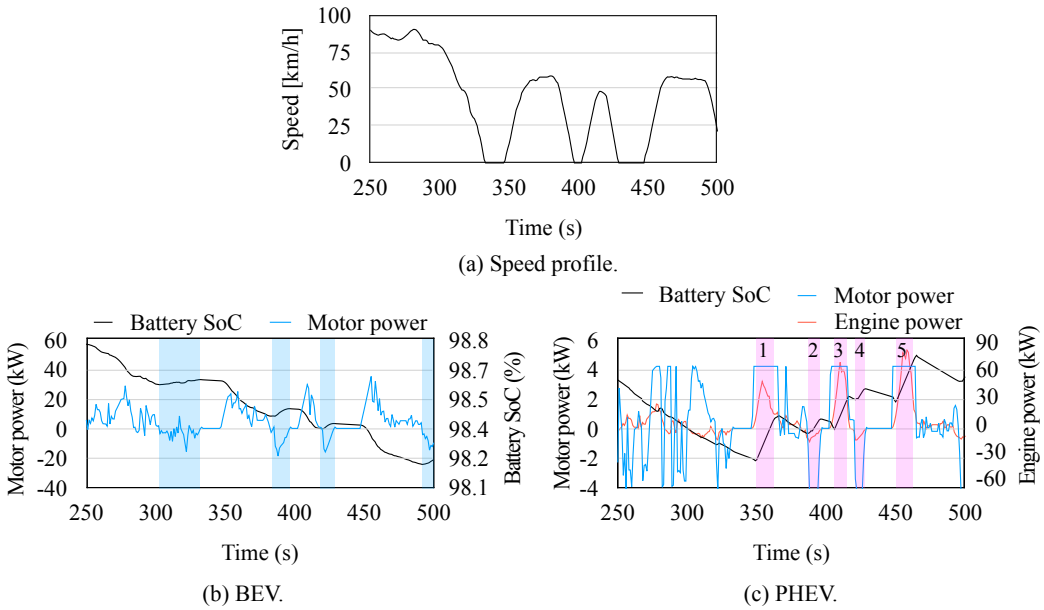

(a) Speed profile.

(b) BEV.

(c) PHEV.

Fig. 3.3 Battery charging by (b) regenerative braking by a motor and (c) regenerative braking by a motor and electricity generation by an engine.

Battery usage analysis

The battery SOC of the BEV and PHEV is discharged or charged during the test driving because of energy consumption for accelerating or continuing vehicle speed and energy regeneration as shown in Figure 3. Because the degradation of the battery pack is strongly dependent to the charging and discharging cycles, battery usage is defined as the total number of absolute ampere-hours Ah during service time, as set forth in the following equation:

$$Ah = \int_0^T |I(t)|dt \tag{3.7}$$

where I is battery current, and T is driving/charging time. Accordingly, the maximum number of ampere-hours in battery life is Ah_{max}. The ratio of battery fade C_f and $C_{f_{max}}$ in (3.3) is assumed to be approximated as the ratio of battery usage A_h and $A_{h_{max}}$.

Table 3.1 Energy consumption and cost

	PHEV	BEV
Electrical energy, E_e (Wh)	128.3	1972.4
Gasoline energy*, E_g (g)	645.3	0.0
Cost by electricity, $E_e \cdot p_e$ ($)	0.048	0.740
Cost by gasoline, $E_g \cdot p_g$ ($)	0.950	0.0
Total cost	0.998	0.740

* the quantity of gasoline is given in grams

In addition, Ah_{index} is defined as the ratio of the total ampere-hours Ah in a certain period of service time to the nominal capacity Ah_b of battery pack:

$$Ah_{index} = \frac{Ah}{Ah_b} \tag{3.8}$$

The consumption and generation for the driving test and battery usage during the driving test is summarized in Table 3.2. The BEV consumes nearly four times more electrical energy than the PHEV, which also uses gasoline energy. However, the PHEV shows a higher battery usage than the BEV, although the total variation in SOC is smaller due to the frequent charging phases and the lower discharged energy of the PHEV battery.

Table 3.2 Battery usage analysis

	PHEV	BEV
Discharged energy (Wh)	544.0	2261
Charged energy (Wh)	415.7	288
Total energy (Wh)	959.8	2549
Ah_{index} (%)	10.9	5.1
Total SOC variation	1.5	3.9

Battery cost analysis

In this subsection, the battery costs are analyzed and discussed for a sake of comparison based on the battery usage data reported in Table 3.2 for the UDDS test cycle. Battery prices are steadily falling due to mass production and advance in lithium-ion manufacturing technology. The battery price including cell price and cell-to-pack price becomes 132 $ in 2021. So, it is assumed that the replacement cost of a whole battery pack of Model 3, which consists of four battery modules, is 6,600 $. Conversely, the replacement cost for the PHEV battery (8.8 kWh) is assumed to be 1,162 $ by scaling down. The battery warranty period is 8 years for Model 3 [122]. The minimal daily cost $c_{d_{min}}$ is obtained by dividing the total battery cost by the warranty period. To obtain the actual cost per day, two driving tests a day are considered. Results are summarized in Table 3.3.

Table 3.3 Battery price and warranty

	PHEV	BEV
Total battery price ($)	1,162	6,600
Battery energy (kWh)	8.8	50
Warranty (year)	8	8
Optimal daily usage cost ($)	0.398	2.260
Actual daily usage cost ($)	0.633	1.683

Figure 3.4 shows a comparison between c_{min} and c_a for BEV and PHEV, respectively. Indeed, c_a is always lower than c_{min} in the case of the BEV as shown in Figure 3.4(a); this means that the BEV battery is underused in this test case. An additional daily driving time of about 15.7 minutes, at those test conditions, is required to achieve the optimal daily cost from a warranty perspective for the BEV under test. Conversely, the PHEV battery is overused, as shown in Figure 3.4(b). In fact, c_a is higher than c_{min} because of the more frequent charging and discharging cycles, which accelerate battery degradation. For this reason, the replacement of the PHEV battery is expected before the warranty expiration period.

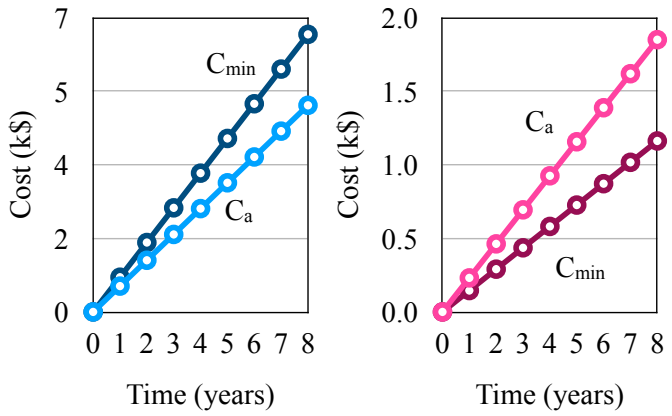

(a) BEV. (b) PHEV.

Fig. 3.4 Battery cost comparison between c_a and c_{min} in (a) BEV and (b) PHEV.

Battery aging analysis by driving profiles

In this section, the battery usage cost have been evaluated on six driving cycles, in addition to the UDDS cycle, as listed in Table 3.4. These cycles are also defined by the EPA Vehicle Chassis Dynamometer Driving Schedules [99] to test a vehicle in the following scenarios:

1. Inspection & Maintenance (IM240), which is commonly used for roadside testing.
2. Federal Test Procedure (FTP) also known as EPA75. This test is based on the UDDS test, with the final part (t =505 s) being the same as the initial one.
3. Highway Fuel Economy Test (HWFET), for testing highway driving conditions with a speed limit of 60 mph.
4. New York City Cycle (NYCC), for low speed and stop-and-go driving.
5. High acceleration, deceleration and speed driving (US06), as supplemental FTP driving schedule.
6. Air Conditioning supplemental FTP driving schedule (SC03).

Table 3.4 reports the total distance, driving time and average speed of each test. In this case, the distance and average speed are reported in miles and miles per hour

(mph), respectively, in order to maintain the original units of measurement and avoid any approximation from converting miles to kilometers.

Table 3.4 List of driving cycles

Name	Distance (miles)	Driving time (s)	Avg. speed (mph)
UDDS	7.45	1369	19.59
IM240	1.96	240	29.38
FTP	11.04	1874	21.2
HWFET	10.26	765	48.3
NYCC	1.18	598	7.1
US06	8.01	596	48.37
SC03	3.58	596	21.55

Similar to the UDDS test, for the battery usage cost analysis it is assumed two driving tests for each daily driving cycle. Figure 3.5(a) shows the battery energy consumption by the BEV, which corresponds to the energy for driving. The battery usage for the US06 test is higher than the dashed line because the battery consumes energy with acceleration, deceleration and high-speed driving on highway. Figure 3.5(b) shows the relationship among the driving cycles with respect to the driving distance and PHEV battery usage. The dashed line refers to a baseline passing UDDS, which is a typical city driving. Most driving cycles are on or near the dashed line, except US06 and HWFET. The latter requires less battery energy because of the long driving time without high acceleration/deceleration. So, in this case, there is less battery charging by regenerative braking and battery discharging due to vehicle acceleration. US06 is between the dashed line and HWFET because this driving cycle is a mix of highway driving and city driving.

Figure 3.6 shows the battery cost comparison only for the following driving cycles: FTP, HWFET, NYCC and US06. The reason is that the IM240 test is the "Inspection & Maintenance Driving Schedule", whereas SC03 is the Air Conditioning supplemental FTP driving schedule, that is "Speed Correction Driving Schedule". Accordingly, the details of these two tests are not included in Figure 3.6, although the main results are reported in Figure 3.5.

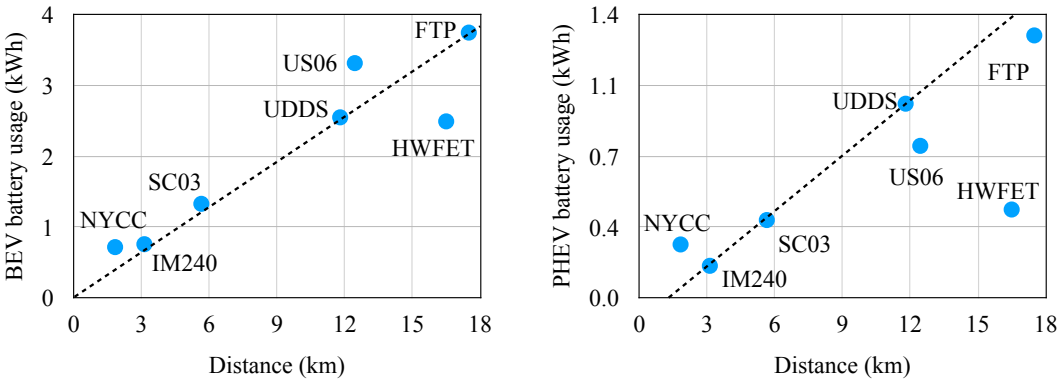

(a) BEV. (b) PHEV.

Fig. 3.5 Driving cycle comparison by battery energy vs. travel distance.

The FTP is a 31-minute light-duty vehicle driving test. In this case, the usage of the BEV battery is just slightly higher than the optimal one. Therefore, the battery warranty is almost adequate. Conversely, the PHEV battery is extremely overused, so that a replacement will be required twice during the warranty period. In fact, the acceleration and deceleration phases are even more frequent than in the UDDS test.

HWFET is a short (less than 13 minutes) highway vehicle driving test. In this case, because the usage of PHEV and BEV batteries is less than optimal the related costs are also less than optimal. For the PHEV, the battery usage cost is lower than optimal because there are fewer acceleration and deceleration phases during highway driving than during city driving.

NYCC is a 10-minute driving test under low speed and stop-and-go traffic conditions. Due to the short driving time, the degradation of PHEV and BEV batteries is less than optimal. However, the use of these batteries is relatively high because of the frequent stop-and-go driving patterns.

US06 is also a 10-minute driving cycle but, compared to NYCC, US06 consists of greater acceleration, deceleration and, in general, speed. In this case, the use of the BEV battery is close to optimal from a cost perspective. This is true also for the PHEV battery, but as a consequence of the short driving time.

In summary, the usage cost of a PHEV battery is greater than optimal in all situations in which frequent stops and acceleration/deceleration phases occur. Conversely, the usage cost of a BEV battery pack is close to optimal in all driving conditions. However, this result depends on daily travel distance, whose optimal value depends

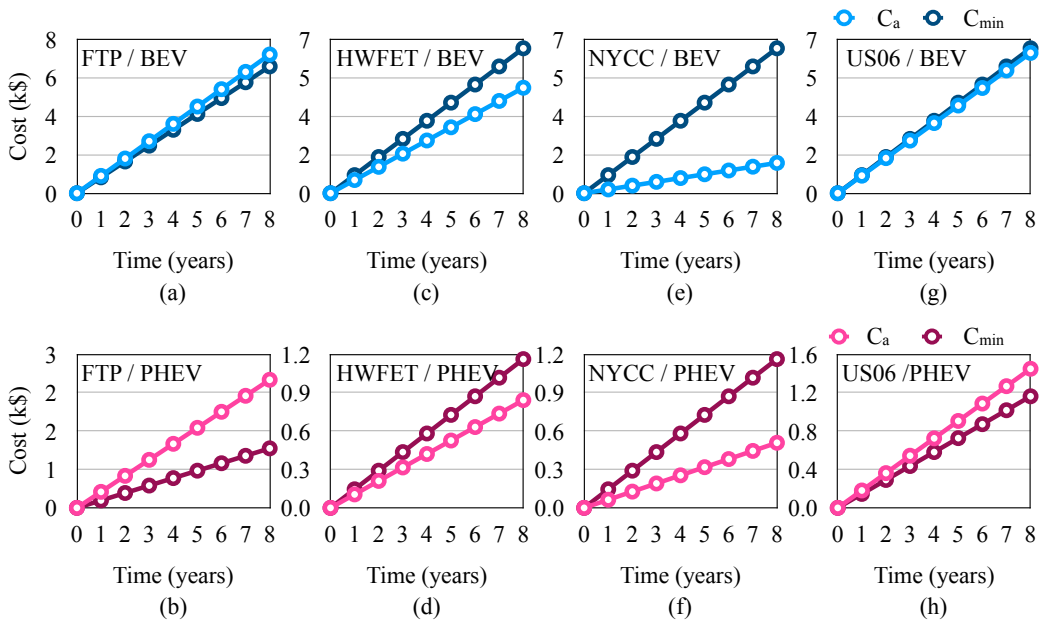

Fig. 3.6 Battery cost comparison between c_a and c_{min} for four different driving cycles.

on driving condition and scenario. Accordingly, a further step is required to evaluate the best use of these batteries. Figures 3.7(a) and 3.7(b) show the optimal number of cycles and travel distance in a day in order to use the battery optimally for the BEV and PHEV, respectively, under test conditions.

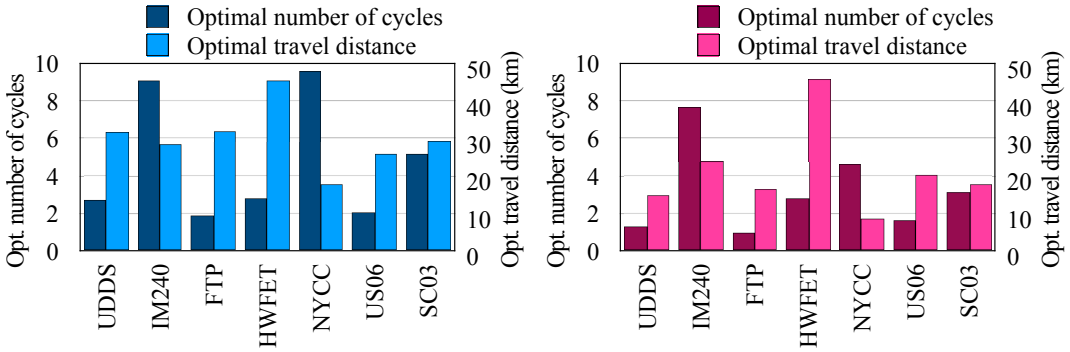

Fig. 3.7 Optimal number of cycles and travel distance.

In general, the optimal number of cycles of a driving test is inversely proportional to its driving distance: if this distance is too short, it is necessary to drive more to consume the battery optimally. The optimal number of cycles for PHEVs is generally less than that for BEVs, even about half in the case of UDDS and NYCC, except for HWFET.

3.2 Efficient use of charging stations for EVs

3.2.1 Introduction

The impressive growth in the production of EVs and the accompanying installation of new electric charging stations are attracting the attention of electric utilities and researchers. This new dynamic scenario presents us with unprecedented challenges. Therefore, optimization algorithms and methods have been developed, especially in the last decade, to take into account power consumption in distribution networks as well as power costs and charging time of EVs. Solving the problems that arise with EV mobility, such as excessive time spent at public stations and equitable distribution of charging requests over time, can be addressed using real-world data [123]. However, some situations can only be analyzed through accurate simulations. For example, analyzing all possible traffic conditions, the impact of some power outages on smart grids, and planning new stations to meet excessive demand for charging services in a distribution network require predictive methods. In addition, the study of general driver behavior also requires a virtual simulation environment. In this context, *range anxiety* is one of the most common attitudes of drivers toward EVs [124]. It concerns the driver's uncertainty about being able to complete the expected trip with the battery as the only energy source. Indeed, BEVs generally have limited range compared to conventional vehicles with gasoline or diesel engines [95]. And although the number and spatial distribution of charging stations are constantly being optimized to meet the ever-increasing demand for electricity for EVs, the infrastructure sometimes still falls short of expectations. Figure 3.8 shows the current prominent locations for charging points, with most charging typically taking place in residential installations.

This work reports some results on the impact of EV charging demand variations on the instantaneous performance of a power grid in accordance with the different behaviors of electric vehicle drivers based on range anxiety. The simulations were performed using an agent-based model (ABM). This model allows the characterization of different scenarios to analyze the impact of infrastructure and driver attitudes on EV charging.

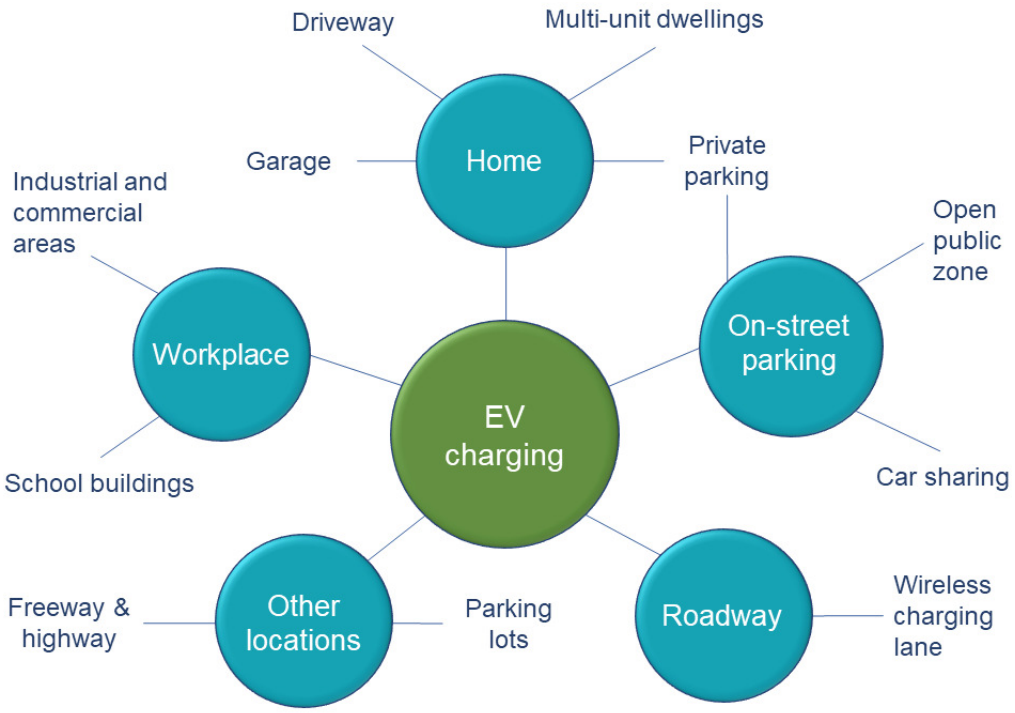

Fig. 3.8 Prominent locations for EV charging installations. © 2021 IEEE.

3.2.2 Background and related work

Today's two most significant barriers to adopting electric vehicles, especially electric cars, are still (i) the maximum distance an electric car can travel on battery power alone and (ii) recharging time, which is usually on the order of a few hours. Although great strides are being made in fast charging, efficiently recharging batteries in just a few minutes remains one of the most critical goals in the automotive sector. These long electrical recharges over a prolonged period can easily lead to overlapping requests for charging stations, thus the possibility of momentary power peaks from the grid [125]. Generally, this scenario has two different objectives: (i) optimal power distribution in a smart grid and (ii) optimal charging of EVs from an operational cost perspective.

Optimal power distribution

First, policies are needed that favor flexibility and distribution of electricity demand from charging stations, which should be as uniform as possible over time [126, 127].

To this end, possible scenarios for integrating EVs into electricity grids can be simulated and analyzed in advance using models. These can help in choosing load forecasting strategies based on charging behavior [128] and then optimization [129]. They are generally based on mathematical methods [130, 131] and computational methods [132]. Among the latter, agent-based models are of great use for the study and simulation of complex systems. This is the case, for example, with the mobility of an EV fleet [133–135] and the associated impact on a power grid [136]. In this context, an ABM developed using NetLogo [137], an open-source tool from Northwestern University, has recently been proposed [138]. It focuses on implementing an optimal infrastructure only to predict the charging demand of a 24-hour EV mobility. The present work differs from this study in its long-term analysis, i.e., a 300-day simulation of mobility for each assumed scenario, where each EV is generally independent from the others in terms of energy consumption and daily mileage. In addition, this work focuses on optimizing the energy demand of an existing charging infrastructure connected to a network rather than optimizing the location of new stations.

Another multi-agent model that incorporates customer behavior was also recently proposed [139]. It simulates a one-year time interval, including weather conditions and customer satisfaction with charging service over time. Although the model defines a threshold for the battery SOC (i.e., SOC_{Limit}, a constraint on the decision to charge the battery), there is no description of the possible decisions for different values of this variable and the resulting outcomes.

Therefore, in the literature, many algorithms and methods exist to optimize power consumption in power networks with charging stations. They consider different situations according to different constraints [131, 140], in particular, battery capacity and charging rates [141, 142], and also the location of newly planned stations [123]. Generally, these techniques are based on the analysis of real data collected from charging stations and/or each electric vehicle. The latter data source seems to be better suited for faster prediction but has the disadvantage that the habits of charging service users are less confidential [143]. Other techniques also analyze EV mobility and parking patterns as optimization keys to flatten the load profile of a grid [134, 127] and the use of auxiliary energy storage to balance demand flexibility [144].

Optimal EV charging

Methods for optimal charging from the point of view of the cost of owning an electric vehicle usually take into account the battery SOC, the time-of-use (TOU) price [145], charging current [141], minimizing battery aging [146], and quality of service [147] as critical factors. In general, the predictive models and decision-making methods for these optimizations are based on well-known techniques such as dynamic programming [130], Markov chain [142], fuzzy theory [129], neural networks [148], and ABMs as mentioned previously.

3.2.3 Model

The model was developed in NetLogo [137], a tool that allows the simulation of multi-agent systems by developing program code in an agile way. It includes special libraries for describing the behavior of individual agents and their interactions and defining a graphical user interface.

Figure 3.9 shows the interface of the proposed ABM. It contains four sliders to set the following variables: the number of charging stations, the charging power, the number of EVs, and the maximum SOC of a battery at initial charging. The latter is the threshold that defines the maximum SOC of the battery of an EV before it is parked at any station for recharging. In other words, this variable is a constraint that obliges an EV to use the recharging service only when the SOC of its battery is less than or equal to this threshold.

The interface also includes nine data monitors, particularly for real-time display of key simulation values such as the maximum instantaneous power of the grid, the number of occupied stations, and the number of stations supplying power to any EV. Indeed, a station may be occupied by a vehicle that is no longer charging (i.e., overstay) since its battery pack has already reached 100% SOC. In this case, the station is occupied but is not supplying power. At the bottom of the interface, there is a window for two different plots. These graphs concern the instantaneous power of the EV grid in the simulation test and the average SOC of all EVs that are not parked at a charging station so that a comparison of the trend of these two quantities is possible.

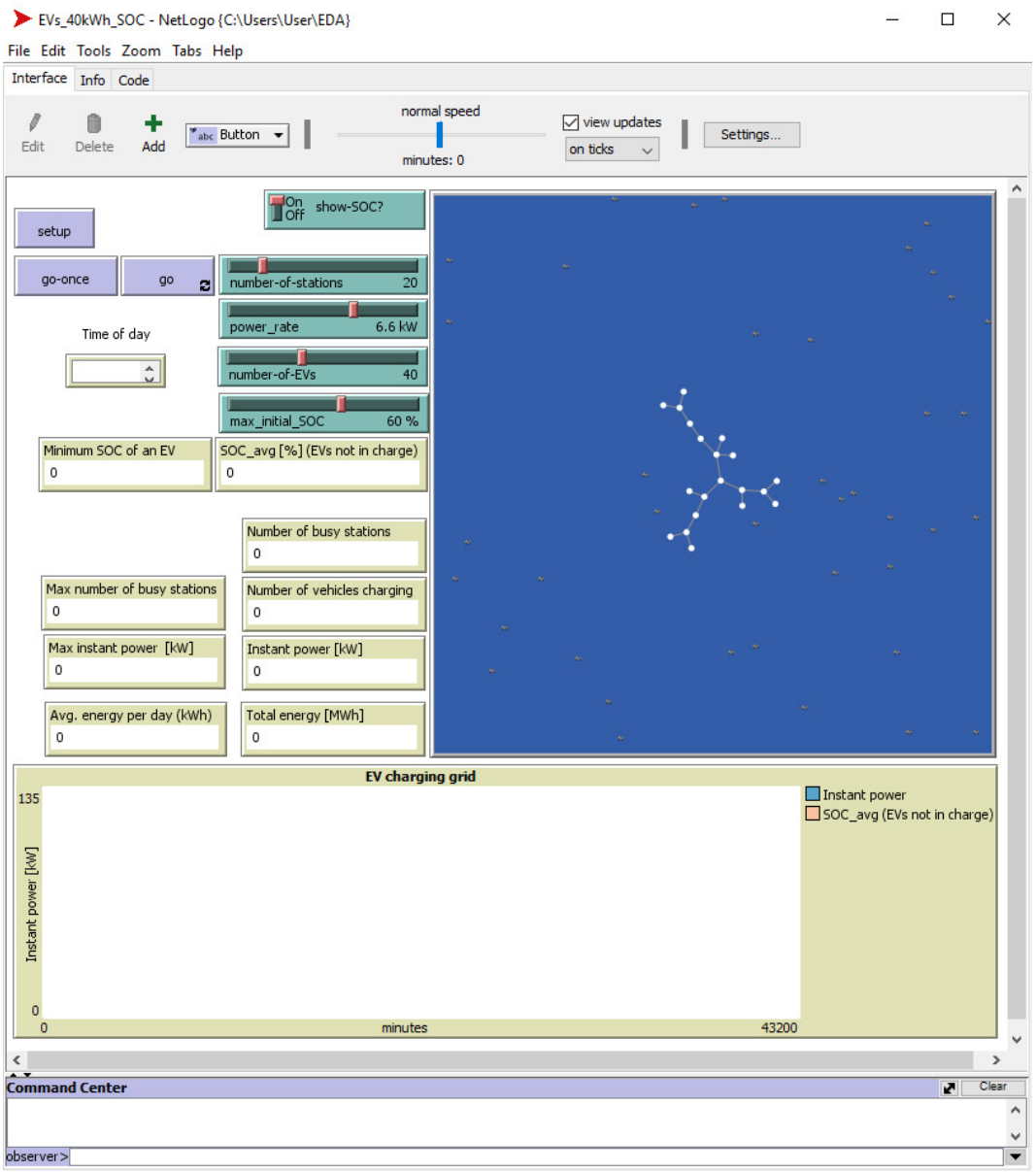

Fig. 3.9 The NetLogo interface developed for the proposed model.

The 24 hours are divided into two time windows: during the day from 7:00 a.m. to 7:00 p.m. and at night from 7:00 p.m. to 7:00 a.m. the next day. When an electric car is parked at a charging station during the night, after its battery is fully charged, it remains there until the next morning. Moreover, mobility at night is minimal compared to daytime, but not completely absent. So all the restrictions serve only to create the typical conditions for EV use.

3.2.4 Results

An ABM was developed using NetLogo 6.1.1, allowing user-defined variables to configure various simulation scenarios. Table 3.5 shows the main settings of the model. In this case, the number of charging stations and EVs are 20 and 40, respectively. These values were set to ensure the broadest possible coverage of possible scenarios and to avoid saturation during the simulation. The total energy of the battery pack of each EV is a preset variable defined in the program code; it is 40 kWh. The charging power is set at 6.6 kW and corresponds to the power of the charger on board each vehicle. Nevertheless, the actual charging power is lower than this value due to the efficiency, so a full charge (from 0 to 100% SOC) of a 40-kWh battery pack takes about 7.5 hours.

Table 3.5 Model parameter setting. © 2021 IEEE.

Parameter	Value
Charging stations	20
Electric vehicles	40
Battery pack	40 kWh
On board charger	6.6 kW
SOC threshold	from 10% to 60% (step 10%)

The possible scenarios are indicated by the maximum SOC threshold ranging from 10% to 60% with a step size of 10%. For each scenario, 10 simulations of 30 days each were performed. In each simulation, each vehicle's initial battery SOC setting and the battery depletion over time are primarily random. In this way, the behavior of each vehicle is independent of another, allowing this model to generate all the situations required for a comprehensive analysis through a stochastic approach.

Peak power

Figure 3.10 summarizes the results regarding the range of maximum peak power during all simulations for each scenario. A larger value of the battery SOC at the beginning of a charging phase generally leads to a higher maximum achievable power. In addition, the range (see the vertical segments) and the mean (see the horizontal markers) of the maximum peak power tend to increase. Nevertheless, the mean is almost constant at two different levels, considering the low and high

values of the SOC threshold (i.e., $\leq 30\%$ and $\geq 40\%$, respectively). In any case, the attitude of drivers of electric vehicles to recharge their vehicles when the batteries have a medium or high SOC leads to a greater number of service requests, albeit for a shorter time compared to the recharge time of the batteries at a low SOC level. This situation leads to greater instability and, thus, uncertainty in a power grid.

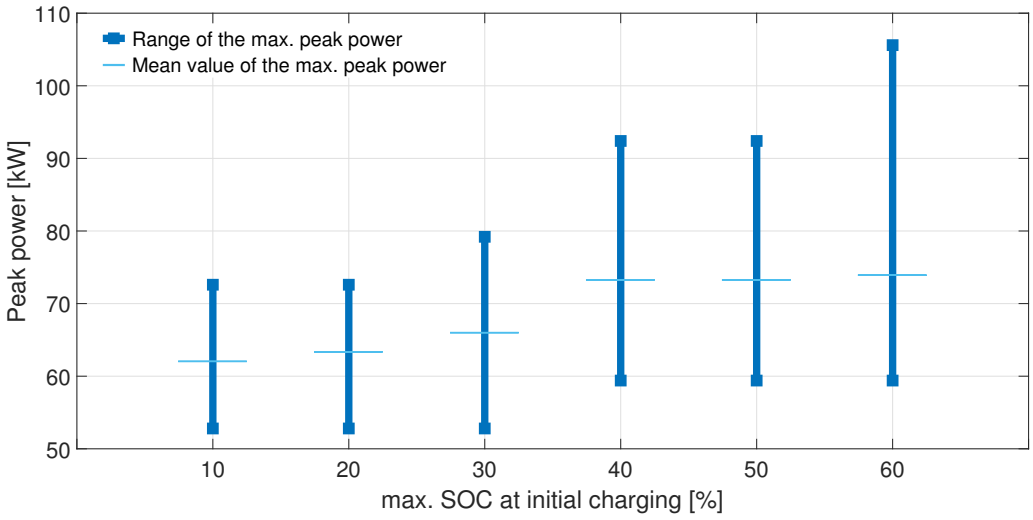

Fig. 3.10 Peak power for different thresholds of battery SOC. © 2021 IEEE.

For clarity, Fig. 3.11 gives all the results regarding the maximum peak power for each simulation run. Indeed, it is also important to analyze the probability of high peak power based on the number of events during the simulations. Although relatively low power peaks are possible in each scenario, this map shows that the probability of higher values of peak power increases as the threshold value of SOC increases.

Charging stations

As for the impact of EV drivers' attitudes toward charging, Fig. 3.12 shows (i) the mean of the maximum number of stations simultaneously charging EVs and (ii) the mean of the maximum number of occupied stations, which include the stations with EVs in the process of recharging and the stations with parked EVs after the end of charging. In the first case, the trend is similar to the mean of the maximum peak

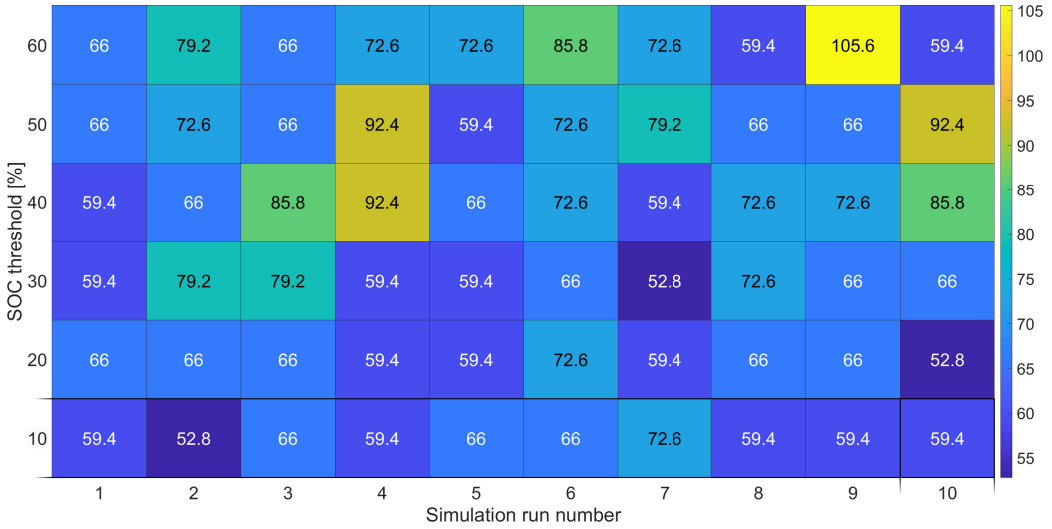

Fig. 3.11 Maximum peak power [kW] during each simulation. © 2021 IEEE.

power. These results (blue dots) are primarily grouped in two different value levels, considering low and high values of the SOC threshold, respectively.

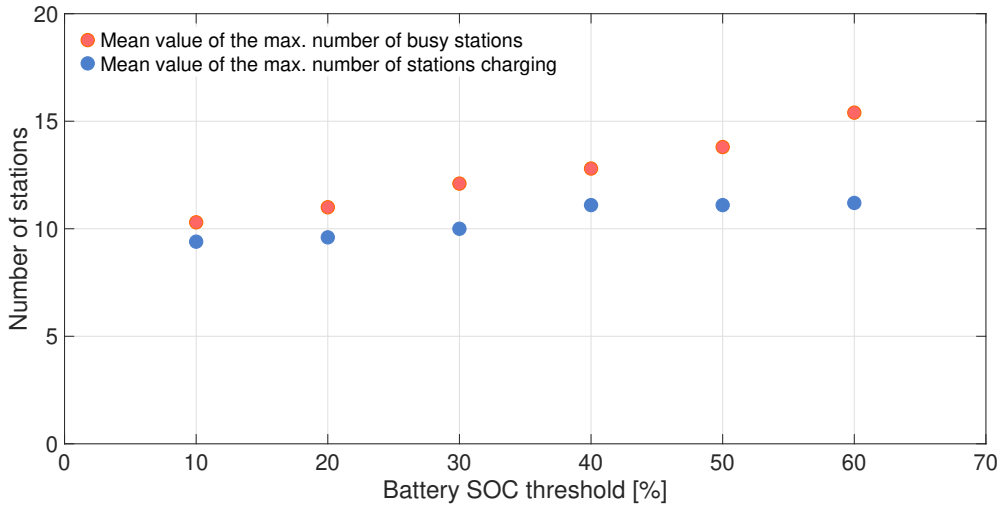

Fig. 3.12 Mean maximum number of stations for different SOC thresholds. © 2021 IEEE.

On the other hand, a monotonically increasing function is more evident when analyzing the busy stations (orange dots). In this case, the trend is almost quadratic, according to the following relation:

$$N_b = 0.7321e^{-3} \cdot x^2 + 0.4761e^{-1} \cdot x + 9.79 \tag{3.9}$$

In (3.9), N_b is the mean of the maximum number of occupied stations simultaneously for each scenario, and x is the maximum SOC of EV batteries at the first recharge. This function concerns the analysis of occupied stations only for the range of battery SOC from 10% to 60%. It is generally rare for an EV with an initial battery SOC charge outside this range, especially considering that drivers' range anxiety can reach higher stress levels when the battery is nearly depleted and that battery aging generally increases at high SOC values [146]. In addition, the distance between the two graphs in Fig. 3.12 tends to increase as the SOC threshold increases. This means that, in general, a larger value of the initial SOC in EV charging leads to a larger probability of station unavailability, so more stations are needed to efficiently meet the energy demand of the same fleet from a quality of service perspective. This drawback should be addressed by better analyzing the causes that lead EVs to remain parked beyond charging hours. However, this is beyond the scope of this work.

In this context, η is defined as the efficiency in the use of stations as follows:

$$\eta = \frac{\max(S_p)}{\max(S_b)} \tag{3.10}$$

In (3.10), S_p is the number of stations simultaneously supplying power to EVs, while S_b is the number of stations utilized. These parameters were evaluated during all scenarios' simulations, with a sampling time of 1 minute. Accordingly, η=1 if each occupied station charges a vehicle. Otherwise, it is less than 1 in the case of overstay of any EV. Figure 3.13 shows the values of η for each of the ten simulation runs considered in each scenario and uses different shades of blue for quick visual analysis. Table 3.6 gives in summary form only the minimum and maximum value of η for each scenario. It is worth noting that both values tend to decrease with an increase in the SOC value at the first recharge. In this case, 40% is the maximum threshold value of SOC to reach an efficiency of 1 or close to 1 with a high probability. Conversely, η could be less than 0.7 for SOC thresholds of 50% and 60%. This effect can be explained by the fact that the larger the SOC value of an EV battery at the beginning of each charging session, the higher the frequency of service requests at charging stations. Therefore, the SOC threshold value may also represent the level of range anxiety in this context.

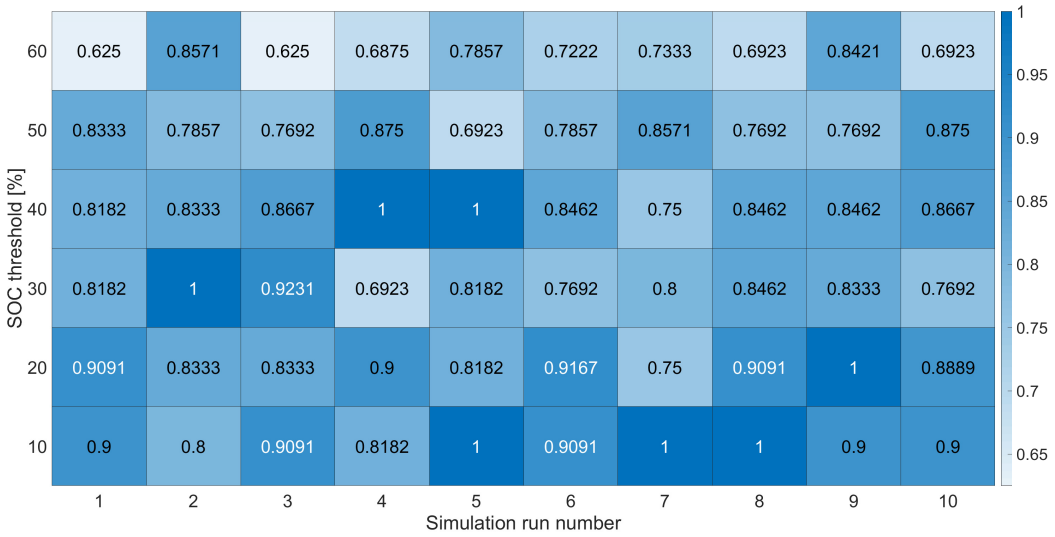

Fig. 3.13 Efficiency η obtained from each simulation. © 2021 IEEE.

Table 3.6 Efficiency in the use of stations. © 2021 IEEE.

SOC threshold [%]	η	
	min.	**max.**
10	0.8000	1.000
20	0.7500	1.000
30	0.6923	1.000
40	0.7500	1.000
50	0.6923	0.8750
60	0.6250	0.8571

Discussion

First, the results suggest that the attitude of EV drivers to charge their vehicles with an initial SOC value of the battery pack higher than 30% may lead to greater uncertainty in predicting electricity demand and that a value greater than 40% could drastically degrade optimized infrastructure use. This result shows that the impact is generally different when considering the probability of high peak power and that of station utilization, although the trend is generally very similar.

Figure 3.14 shows two snapshots of two simulations at different SOC thresholds: one at 20% and the other at 60%. The plots are of the instantaneous power of the EV grid and the average SOC of all vehicles not parked at a charging station. One

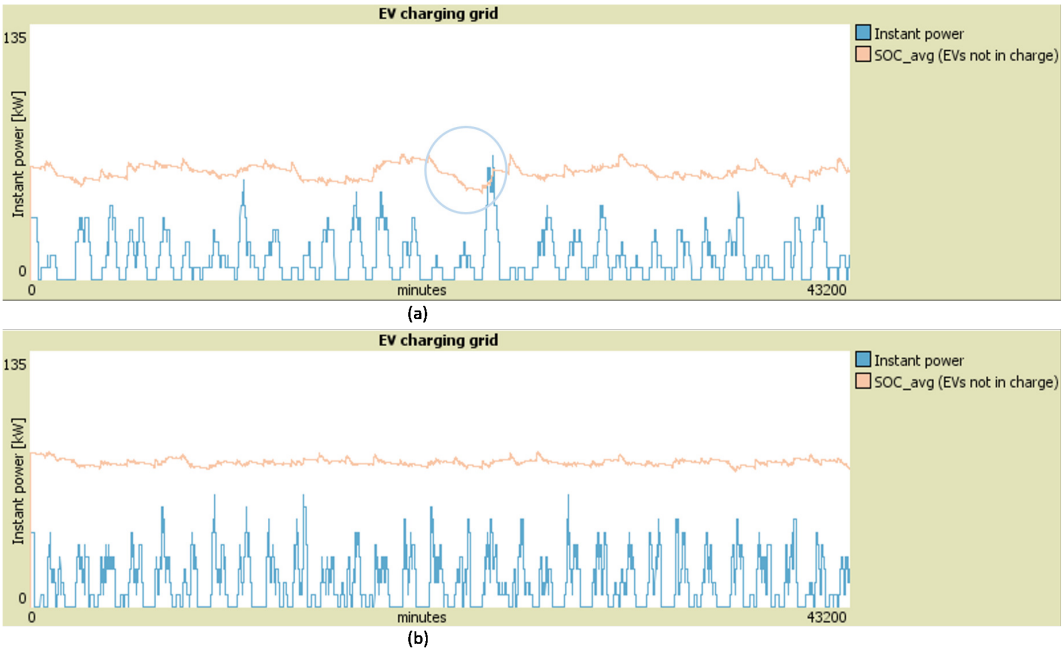

Fig. 3.14 Grid instant power and SOC_{avg} of the EV fleet in two 30-day simulations: max. SOC threshold at 20% (a) and 60% (b). © 2021 IEEE.

observation is that high power peaks tend to follow the longer downward phase of the fleet's average SOC value, as in the example in the circled area of Fig. 3.14(a). Moreover, a larger fluctuation of the average SOC value over time leads to a larger probability of very different peak power values. On the other hand, a stable or flat trend of SOC, as shown in Fig. 3.14(b), significantly improves the stability of peak grid power values.

Chapter 4

Solar Energy Analysis

Some of the work described in this chapter was also previously published in [149].

4.1 Spatial analysis of solar irradiation

4.1.1 Introduction

In an increasingly global world where energy has become the subject of much research, there is still much room for improvement in predicting both energy consumption and the actual contribution of renewables to the overall energy budget. For example, the rapid development of smart grids and the continuous growth of services (e.g., charging stations for electric vehicles) make planning new installations and accurate prediction of energy consumption at regional and national levels difficult, especially for long-term forecasts [150]. In addition, rapid technological change makes it increasingly challenging to perform accurate and rapid analyses for future investments, especially for people who are more economically than technically savvy. In this context, quantifying communities' and nations' solar photovoltaic (PV) potential is becoming increasingly important for their energy self-sufficiency [151]. In particular, the goal of zero energy buildings (ZEBs) engages both researchers and investors to analyze new renewable source installations and develop models to predict electricity load, in addition to analyzing energy efficiency in existing residential and commercial buildings [152, 153].

In this scenario, machine learning, a branch of artificial intelligence (AI), has attracted the attention of many researchers looking for more accurate predictive models in various application areas such as physics, medicine, and economics. Thus, intelligent computational correlation analysis of experimental data is a common task, particularly through the use of regression models that best fit such data [154, 155]. Building these models depends primarily on selecting the most influential parameters (i.e., descriptors) for particular processes.

This chapter describes a nonlinear compact regression model for the geospatial analysis of solar radiation based on only two predictor variables: latitude and mean monthly temperature. Finally, the results are presented with the full data sets in Appendix B.

4.1.2 Background and related work

In the era of Big Data analytics, more accurate and complex methods based on statistical data, such as machine learning techniques, are being proposed in the literature. Among the supervised learning methods, regression-based techniques are the most commonly used [156]. Typical models include linear regression (LR), support vector machine (SVM), commonly referred to in this context as support vector regression (SVR), and Gaussian process regression (GPR) [153, 157, 158]. A comparative study of different machine learning techniques is reported in [159].

Nowadays, artificial neural networks (ANNs) are used in many application areas, even for energy prediction [159, 160]. ANNs are generally used in applications where a large amount of data is available to determine the function that best characterizes the trend of that data; this scenario usually occurs in time series analysis [150, 161]. Unfortunately, there are cases where the number of available data is limited, and these models can easily lead to a lack of accuracy. Nevertheless, polynomials are often used in ANNs. For example, [162] has proposed the modeling of cyber systems by multilayer networks of nonlinear function blocks (i.e., nodes), each having only two inputs for a second-order polynomial function with 6 coefficients or weights (i.e., a_i, i from 0 to 5), as follows:

$$y = a_0 + a_1 x_1 + a_2 x_2 + a_3 x_1^2 + a_4 x_2^2 + a_5 x_1 x_2 \tag{4.1}$$

In this case, two or more cascaded nodes of different layers form higher-order polynomials. However, simpler and more compact models are usually preferred when the estimation accuracy is comparable to that of ANNs, especially in the case of scattered data.

Linear regressions are first-order polynomials. They can be bilinear or trilinear, depending on the number of input arguments (i.e., 2 or 3, respectively) [163]. For example, a linear regression model was proposed in [164] for the monthly mean value of solar radiation H_m as follows:

$$H_m = \alpha + \beta_1 \cdot T + \beta_2 \cdot \phi + \beta_3 \cdot \lambda \tag{4.2}$$

In (4.2), T is the monthly mean air temperature, ϕ and λ are the latitude and longitude, respectively, of a given location, α is the regression constant, while β_1, β_2, and β_3 are coefficients. In general, longitude is a geodata considered for solar radiation analysis in a limited geographical area, such as in the research study reported in [164].

More generally, the combinatorial algorithm considers different versions of the initial first-order equation by adjusting the linear model, i.e., by setting one or more coefficients to zero [37]. The different polynomials obtained in this way can then be included in ANN structures, one for each node in a single layer.

According to [165], the models for solar radiation can be classified as follows:

- Sunshine-based models
- Temperature-based models
- Cloud-based models
- Hybrid-parameter-based models

The Ångström-Prescott equation is the most known sunshine-based model as follows:

$$\frac{H}{H_0} = a + b \cdot \left(\frac{S}{S_0} \right) \tag{4.3}$$

In (4.3), H is the monthly average of daily solar radiation, H_0 is daily extraterrestrial radiation, both on a horizontal plane, S is the monthly average of daily sunshine

duration, and S_0 is the average day length; a and b are coefficients [166]. Recently, hybrid models for solar radiation forecasting have also been developed; a review is given in [167]. However, these models are generally for time-domain analysis and spatial-domain forecasting on a regional/national scale.

For the spatial analysis of the yearly solar irradiation H_y [kWh/m^2] in a given location and at the optimal tilt angle of crystalline silicon (c-Si) PV panels [168] proposed a second-order polynomial with three input arguments and five coefficients as follows:

$$H_y = a_1 \cdot |\phi| + a_2 \cdot h + a_3 \cdot T_{24}^2 + a_4 \cdot |\phi| \cdot T_{24}^2 + a_5 \tag{4.4}$$

In (4.4), ϕ, h, and T_{24} are, respectively, the latitude, altitude, and average daily temperature of a given location. Although this model has a higher number of parameters and coefficients than the proposed one, it is still used to compare the accuracy of the results.

4.1.3 Model

Although modeling methods nowadays are primarily based on statistical data, the approach used here differs in that the correlation of solar radiation with the geophysical aspects of the sites is mainly considered in the modeling. In addition, due to the general preference for compact models, the number of parameters and coefficients was a constraint in the development. The proposed model for estimating the yearly solar irradiation H_y at an optimal tilt angle of the c-Si PV panels at a given site is as follows:

$$H_y = a_1 + \frac{a_2}{T_m} + a_3 \cdot |\phi| \cdot T_m^2 + a_4 \cdot \phi^2 \tag{4.5}$$

In (4.5), T_m is the mean temperature over the year at a given location, ϕ is the latitude, and a_i are the model's coefficients. In practice, this is a second-order polynomial for both variables ϕ and T_m, where $a_3 \cdot |\phi| \cdot T_m^2$ reflects the relationship between temperature and latitude. Regarding the last term, it is important to note that the coefficient a_4 is negative since solar radiation generally tends to decrease for higher and higher latitudes, especially in the areas between the tropics and the Earth's poles.

4.1.4 Results

The proposed model is tested for two very different geographic areas: Europe and Africa. For each of these continents, the data relating to the temperature and solar irradiation of 40 locations were extracted from the Photovoltaic Geographical Information System (PVGIS) by the Joint Research Centre of the European Commission [1]. PVGIS is an online tool for analyzing the solar photovoltaic potential in Europe, Africa, and large parts of Asia and America (PVGIS© European Communities, 2001-2021) [169, 170].

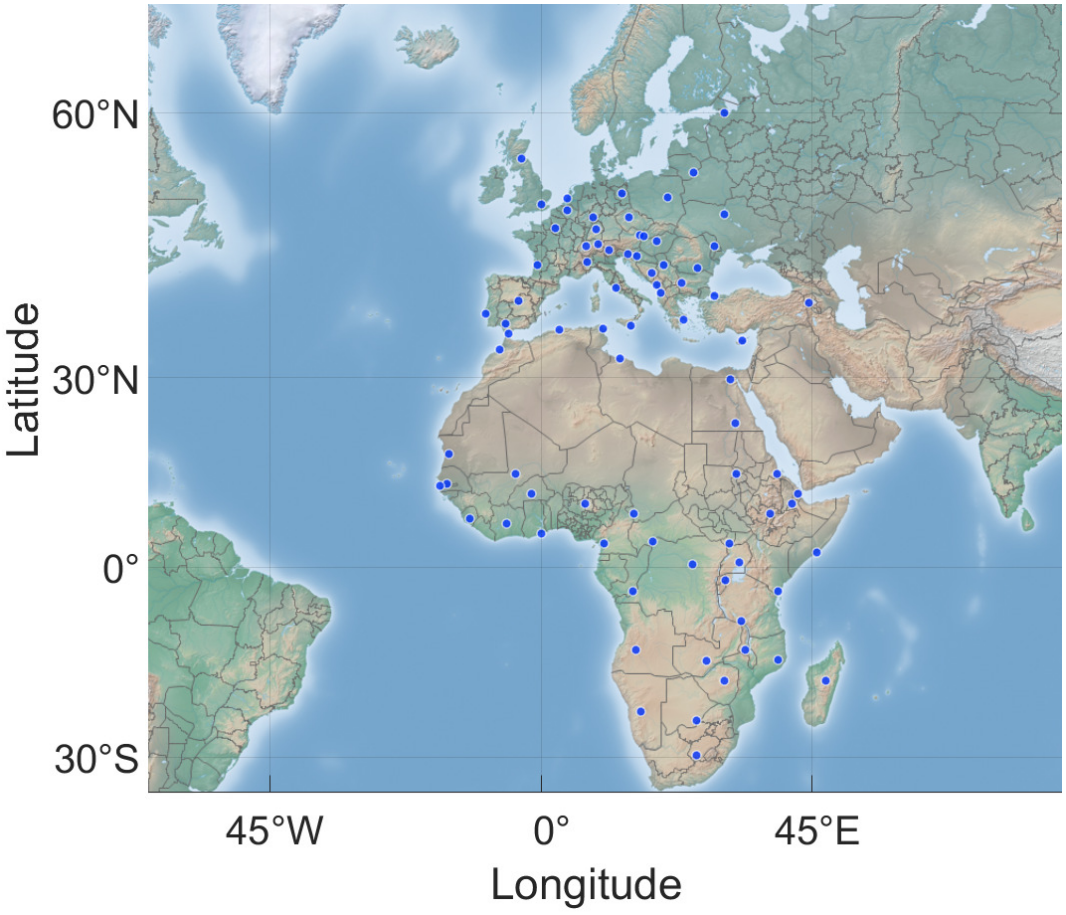

Fig. 4.1 Map with the selected locations in Europe and Africa. © 2022 IEEE.

The selected locations are generally very different from each other, and they span a total latitude of about 90° (from -29.74 to 59.98) and a total longitude of over 60° (from -16.70 to 47.32). Monthly average temperature and in-plane solar irradiation at the optimal slope (i.e., tilt angle) of PV panels were extracted by directly accessing

the PVGIS database through the application programming interface (API) of the tool [171]; the program code is provided in Appendix A.

Figure 4.1 shows the locations (blue dots) on the map of the continents, whereas the specific location names and geodata are reported in Appendix B.

Table 4.1 reports the Pearson correlation matrix (i.e., normalized covariance matrix) of the full data set, which also includes longitude (λ) and altitude (h) in addition to the model parameters ϕ and T_m, and also H_y by PVGIS for all 80 locations. It should be noted that the selection of the temperature and latitude for the model is in accordance with their absolute correlation value with the solar irradiation (i.e., 0.8937 and 0.6900, respectively) and between themselves (i.e., 0.7054).

Table 4.1 Correlation matrix for the geodata of all the 80 locations.

	ϕ	λ	h	T_m	H_y
ϕ	1.0000	-0.2942	-0.6477	-0.7054	-0.6900
λ	-0.2942	1.0000	0.4899	0.0162	0.1193
h	-0.6477	0.4899	1.0000	0.1410	0.3146
T_m	-0.7054	0.0162	0.1410	1.0000	0.8937
H_y	-0.6900	0.1193	0.3146	0.8937	1.0000

For the validation of the model, all the locations are divided into two data sets according to their respective continents: k_1 for Europe and k_2 for Africa. In this way, one data set is used as a training set while the other is used as a test or validation data set for k-fold cross-validation with k=2. Figure 4.2 shows H_y as extracted from the PVGIS database, the estimates of the model, and the two fitting functions of the PVGIS data for Europe (upper graph) and Africa (lower graph), respectively. The analysis of these functions for the feature H_y *vs.* $latitude$ shows the large difference in the data distribution between these two continents. Indeed, the fit function for the sites in Europe is quadratic, while the data distribution in Africa resembles a 6th-order polynomial function. This remarkable dissimilarity further strengthens the validation since the training set is always very different from the test set. Another observation is that the two maxima of the fitting function in the bottom graph practically coincide with the tropics at latitude -23.4° and +23.4°, which is a consequence of the inclination of the Earth's rotation axis. Nevertheless, these values differ for the data set considered here.

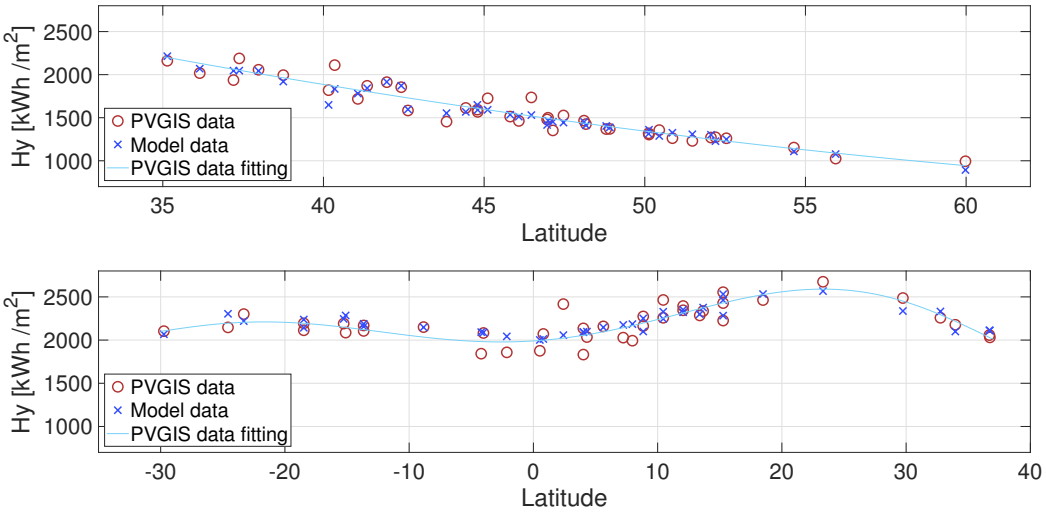

Fig. 4.2 A comparison of the PVGIS data and the results obtained with the proposed model in Europe (upper graph) and Africa (lower graph). © 2022 IEEE.

Table 4.2 gives the coefficients of (4.5) that minimize the root mean square error (RMSE) for the training set, that is, for the data from Europe during the first simulation run and those from Africa during the second simulation run. Just as the distributions of the data are different in the two continents, so are generally the coefficients. The algorithm used to determine the coefficient values is based on the least squares method, but with the condition that at a given search step, the maximum error of the training set is also less than that determined in the previous steps.

The RMSE of the model is 102.75. For comparison, Table 4.3 reports the mean absolute percentage error (MAPE) and RMSE of the proposed two-parameter model and the three-parameter model from (4.4), for which the coefficients are given in [168]. It should be noted that the model proposed here improves accuracy by using only two parameters instead of three, that is, by excluding the altitude of the locations and with only four coefficients instead of five. Nevertheless, these models include the same relationship between ϕ and T (i.e., $|\phi| \cdot T^2$).

Conventional regression models are applied to the same data sets through the same cross-validation procedure to validate the model further. Two different simulations were performed: the first with only two predictor variables (i.e., latitude and temperature), similar to the validation of the proposed model in (4.5), and the second additionally included the altitude of each location as a third predictor variable.

Table 4.2 The coefficients of (4.5) for the 2-fold validation. © 2022 IEEE.

Coeff.	Value		Unit
	k_1 (Europe)	k_2 (Africa)	
a_1	1900	1845	$\text{kWh}\cdot\text{m}^{-2}$
a_2	2103	2300	$\text{kWh}\cdot\text{m}^{-2}\cdot^{\circ}\text{C}$
a_3	0.046	0.049	$\text{kWh}\cdot\text{m}^{-2}\cdot^{\circ}\text{C}^{-2}$ per degree of $\lvert\phi\rvert$
a_4	-0.400	-0.400	$\text{kWh}\cdot\text{m}^{-2}$ per degree of ϕ squared

Table 4.3 Comparison of the model errors. © 2022 IEEE.

proposed model		[168]	
MAPE [%]	RMSE [kWh/m^2]	MAPE [%]	RMSE [kWh/m^2]
4.1	102.75	5.7	129.30

Results obtained by such models using the Regression Learner App by Mathworks [172] are reported in Table 4.4, where 2p and 3p denote the number of predictor variables in the data set, 2 and 3, respectively.

Again, the errors are higher than the error yielded by the proposed model. It is important to note that principal component analysis (PCA) was not applied because it worsened the estimates. In addition, the results obtained with regression trees are not reported since the errors associated with them were generally very high compared to those of the other regression models.

Figure 4.3 shows the characteristic *Temperature vs. Latitude* for all the locations in the data sets. The colors of the dots refer to the solar irradiation extracted from the PVGIS database. Although the trend of feature T vs. ϕ generally follows the trend of feature H_y vs. ϕ, the graph shows an outlier (T_m=14.5 at ϕ=8.84) for the location in Ethiopia as a result of altitude (above 2,000 m a.s.l.). Although the proposed model does not include altitude as a predictor, this outlier is not present in the results; in fact, the absolute error of estimate for this site is 2.9%. This result is another confirmation of the goodness of the model.

Table 4.4 Results obtained by conventional regression models. © 2022 IEEE.

Regression model	RMSE	
	2p	3p
Linear	194.52	167.51
Interactions Linear	136.45	136.47
Robust linear	192.94	167.90
Stepwise Linear	136.45	132.30
Linear SVM	191.38	166.83
Quadratic SVM	146.29	159.33
Cubic SVM	138.13	182.45
Fine Gaussian SVM	212.07	200.77
Medium Gaussian SVM	132.60	123.95
Coarse Gaussian SVM	183.06	187.55
Optimizable SVM	123.45	406.67
Squared Exponential GPR	127.46	127.65
Matern 5/2 GPR	122.48	120.38
Exponential GPR	129.65	111.10
Rational Quadratic GPR	127.44	118.64
Optimizable GPR	120.97	113.51

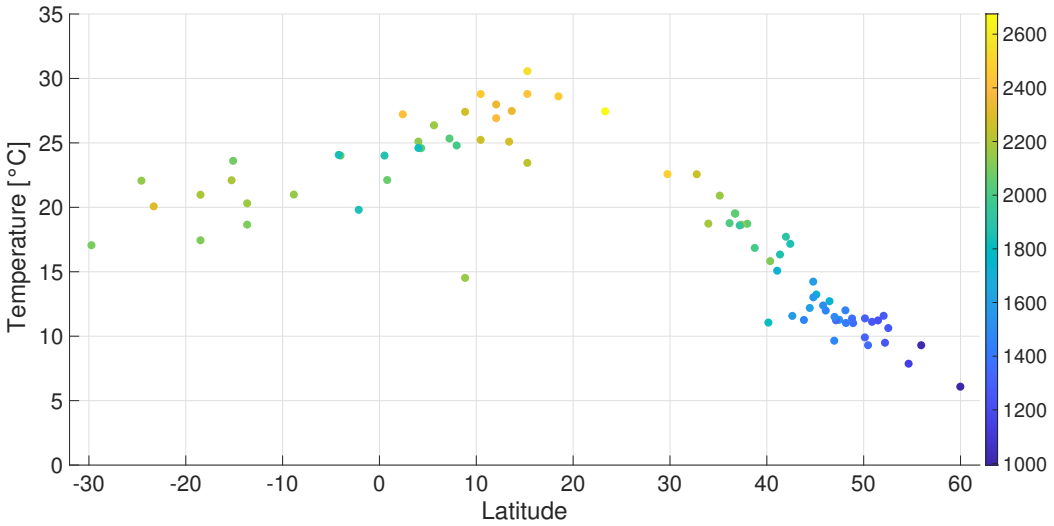

Fig. 4.3 T_m vs. ϕ characteristic for all the locations. © 2022 IEEE.

Chapter 5

Conclusion and Future Directions

To make the analysis and possible optimization of energy resources more accessible to end users, it is necessary to provide compact models with limited parameters and coefficients that allow immediate results. This thesis highlights the opportunity to provide easy-to-use models and tools and confirms the possibility of creating compact models with reasonable accuracy for complex systems.

Since developing new compact models for such systems is not just a matter of model reduction or complexity minimization, a preliminary method is proposed, albeit based on a slight variation of existing data analysis techniques. In particular, the selection of *predictor variables* that best contribute to the definition of the model function describing the characteristics of the *response variable* is based on the use of parametric and/or nonparametric correlation methods. This procedure was applied to solar energy analysis in the field of photovoltaics through the use of Pearson correlation analysis.

Furthermore, the proposed compact modeling approach considers existing models' adaptation and/or extension. In this case, the well-known Peukert's law for analyzing the performance of batteries discharged at constant currents, proposed at the end of the 19th century for lead-acid batteries, has been adapted for the analysis of the performance of alkaline and lithium-based primary batteries also discharged at pulse currents.

In addition, some cost analysis models have been further proposed due to users' attention regarding energy costs. In particular, some simple models have been reported for the analysis and possible optimization of the costs for the use of batteries

in devices (e.g., single cells for sensors) and systems (e.g., battery packs in electric vehicles). Since the performance of the batteries depends on the operating (e.g., temperature) and working (e.g., current) conditions, in addition to the cost models, a method has been provided for comparing the properties of different batteries from their datasheets, in order to choose for a specific application the one which has the lowest total cost. On the other hand, a basic metric for the cost analysis of the wear of battery packs in electric vehicles was proposed; this is based on the characteristics of road route and travel distance.

In future work, the methodology for defining compact mathematical functions should be further outlined, especially for the nonlinear descriptions of the *emergent* properties in complex systems. Furthermore, from an implementation point of view, analytical models should be included in user-friendly tools or apps for their practical use.

References

[1] PVGIS, online tool.
http://re.jrc.ec.europa.eu/pvgis.

[2] Warren Weaver. Science and complexity. *American scientist*, 36(4):536–544, 1948.

[3] Mark E. J. Newman. Complex systems: A survey. *arXiv preprint arXiv:1112.1440*, 2011.

[4] Francis Heylighen. Complexity and self-organization. *Encyclopedia of library and information sciences*, 3:1215–1224, 2008.

[5] Francis Heylighen. Entanglement, symmetry breaking and collapse: correspondences between quantum and self-organizing dynamics. *Foundations of Science*, pages 1–23, 2021.

[6] Nino Boccara. *Modeling complex systems*. Springer Science & Business Media, 2010.

[7] Julio M. Ottino. Engineering complex systems. *Nature*, 427(6973):399–399, 2004.

[8] Silvio Funtowicz and Jerome R. Ravetz. Emergent complex systems. *Futures*, 26(6):568–582, 1994.

[9] Richard Foote. Mathematics and complex systems. *Science*, 318(5849):410–412, 2007.

[10] Enrique Alberto Kremers. *Modelling and simulation of electrical energy systems through a complex systems approach using agent-based models*. KIT scientific publishing, 2013.

[11] Subana Shanmuganathan. Artificial neural network modelling: An introduction. In *Artificial neural network modelling*, pages 1–14. Springer, 2016.

[12] Hiroki Sayama. *Introduction to the modeling and analysis of complex systems*. Open SUNY Textbooks, 2015.

[13] Leo Torres, Ann S. Blevins, Danielle Bassett, and Tina Eliassi-Rad. The why, how, and when of representations for complex systems. *SIAM Review*, 63(3):435–485, 2021.

[14] Venkateswararao Vemuri. *Modeling of complex systems: an introduction*. Academic Press, 2014.

[15] Till Grüne-Yanoff and Uskali Mäki. Introduction: Interdisciplinary model exchanges. *Studies in History and Philosophy of Science Part A*, 48, 2014.

[16] Francesca Lazzeri. *Machine learning for time series forecasting with Python*. John Wiley & Sons, 2020.

[17] Chirag Deb, Fan Zhang, Junjing Yang, Siew Eang Lee, and Kwok Wei Shah. A review on time series forecasting techniques for building energy consumption. *Renewable and Sustainable Energy Reviews*, 74:902–924, 2017.

[18] Ryosuke Jinnouchi, Ferenc Karsai, and Georg Kresse. Making free-energy calculations routine: combining first principles with machine learning. *Physical Review B*, 101(6):060201, 2020.

[19] Bei Sun, Chunhua Yang, Yalin Wang, Weihua Gui, Ian Craig, and Laurentz Olivier. A comprehensive hybrid first principles/machine learning modeling framework for complex industrial processes. *Journal of Process Control*, 86:30–43, 2020.

[20] Clive Dym. *Principles of mathematical modeling*. Elsevier, 2004.

[21] Vince Darley. Emergent phenomena and complexity. *Artificial Life*, 4:411–416, 1994.

[22] Peter Benner, Mario Ohlberger, Albert Cohen, and Karen Willcox. *Model reduction and approximation: theory and algorithms*. SIAM, 2017.

[23] Yemi Ojo, Jeremy Watson, and Ioannis Lestas. A review of reduced-order models for microgrids: Simplifications vs accuracy. *arXiv preprint arXiv:2003.04923*, 2020.

[24] Jon Wakefield. *Bayesian and frequentist regression methods*, volume 23. Springer, 2013.

[25] Yaneer Bar-Yam. A mathematical theory of strong emergence using multiscale variety. *Complexity*, 9(6):15–24, 2004.

[26] Ventana Systems, Inc. Vensim. https://vensim.com.

[27] Powersim Software AS. Powersim Studio. https://powersim.com.

[28] Isee Systems, Inc. Stella. https://www.iseesystems.com/store/products/.

[29] Uri Wilensky and William Rand. *An introduction to agent-based modeling: modeling natural, social, and engineered complex systems with NetLogo*. Mit Press, 2015.

[30] The AnyLogic Company. AnyLogic Simulation Software. https://www.anylogic.com/.

[31] FAME. https://gitlab.com/fame-framework.

[32] Argonne National Laboratory. The Repast Suite. https://repast.github.io/index.html.

[33] Project Mesa Team. Mesa: Agent-based modeling in Python 3+. https://mesa.readthedocs.io/en/stable/index.html.

[34] Center for Connected Learning and Evanston IL Computer-Based Modeling, Northwestern University. NetLogo 6.3.0 User Manual: System Dynamics Guide. https://ccl.northwestern.edu/netlogo/docs/systemdynamics.html, 2023.

[35] Paul Cilliers. Boundaries, hierarchies and networks in complex systems. *International Journal of Innovation Management*, 5(02):135–147, 2001.

[36] Mark Kelly, Mark Fortune, Gilles Bourque, and Stephen Dooley. Toward development of machine learned techniques for production of compact kinetic models. *arXiv preprint arXiv:2202.08021*, 2022.

[37] Hema Rao Madala and Alexey Grigorevich Ivakhnenko. *Inductive learning algorithms for complex systems modeling*. CRC press, 2019.

[38] Paul Gasper, Kevin Gering, Eric Dufek, and Kandler Smith. Challenging practices of algebraic battery life models through statistical validation and model identification via machine-learning. *Journal of the Electrochemical Society*, 168(2):020502, 2021.

[39] Jogesh K. Muppala, Manish Malhotra, and Kishor S. Trivedi. Markov dependability models of complex systems: Analysis techniques. In *Reliability and Maintenance of Complex Systems*, pages 442–486. Springer, 1996.

[40] Steven M. Manson. Simplifying complexity: a review of complexity theory. *Geoforum*, 32(3):405–414, 2001.

[41] Norman R Draper and Harry Smith. *Applied regression analysis*, volume 326. John Wiley & Sons, 1998.

[42] Stefan Pfenninger, Adam Hawkes, and James Keirstead. Energy systems modeling for twenty-first century energy challenges. *Renewable and Sustainable Energy Reviews*, 33:74–86, 2014.

[43] Catherine S. E. Bale, Liz Varga, and Timothy J. Foxon. Energy and complexity: New ways forward. *Applied Energy*, 138:150–159, 2015.

[44] Georges Kariniotakis. *Renewable energy forecasting: from models to applications*. Woodhead Publishing, 2017.

[45] Benjamin Shapiro. Creating compact models of complex electronic systems: An overview and suggested use of existing model reduction and experimental system identification tools. *IEEE Transactions on Components and Packaging Technologies*, 26(1):165–172, 2003.

[46] Alberto Bocca and Alberto Macii. Thermal modeling and analysis of a power ball grid array in system-in-package technology. *Multiscale and Multidisciplinary Modeling, Experiments and Design*, 5(1):31–41, 2022.

[47] Alberto Bocca, Yukai Chen, Wenlong Wang, Alberto Macii, Enrico Macii, and Massimo Poncino. A quantitive analysis of the recovery effect in batteries from datasheets. In *SMACD/PRIME 2021; International Conference on SMACD and 16th Conference on PRIME*, pages 1–4. VDE, 2021.

[48] © 2022 IEEE. Reprinted, with permission, from
Alberto Bocca, Yukai Chen, Alberto Macii, Enrico Macii and Massimo Poncino. Adapting the Peukert equation to batteries discharged at pulse currents. In *2022 International Symposium on Power Electronics, Electrical Drives, Automation and Motion (SPEEDAM)*, pages 64–69, 2022.

[49] Alberto Bocca, Yukai Chen, Alberto Macii, Enrico Macii, and Massimo Poncino. A cost-benefit analysis of batteries for Internet-of-Things applications. In *AEIT 2022 International Annual Conference*, Rome, Italy, October, 3-5, 2022 - ISBN 978-88-87237-55-9, ©2022 AEIT.

[50] M. R. Jongerden and B. R. Haverkort. Battery modeling. Technical Report TR-CTIT-08-01, University of Twente, 2008.

[51] Gregory L. Plett. *Battery management systems, Volume I: Battery modeling*. Artech House, 2015.

[52] Jingyuan Zhao and Andrew F. Burke. Electric vehicle batteries: Status and perspectives of data-driven diagnosis and prognosis. *Batteries*, 8(10):142, 2022.

[53] Kristen A. Severson, Peter M. Attia, Norman Jin, Nicholas Perkins, Benben Jiang, Zi Yang, Michael H. Chen, Muratahan Aykol, Patrick K. Herring, Dimitrios Fraggedakis, et al. Data-driven prediction of battery cycle life before capacity degradation. *Nature Energy*, 4(5):383–391, 2019.

[54] Christoph Nebl, Fabian Steger, and Hans-Georg Schweiger. Discharge capacity of energy storages as a function of the discharge current–expanding Peukert's equation. *Int. J. Electrochem. Sci*, 12(6):4940–4957, 2017.

[55] Noshin Omar, Peter Van den Bossche, Thierry Coosemans, and Joeri Van Mierlo. Peukert revisited–Critical appraisal and need for modification for lithium-ion batteries. *Energies*, 6(11):5625–5641, 2013.

[56] Dennis Doerffel and Suleiman Abu Sharkh. A critical review of using the Peukert equation for determining the remaining capacity of lead-acid and lithium-ion batteries. *Journal of Power Sources*, 155(2):395–400, 2006.

[57] Austin Hausmann and Christopher Depcik. Expanding the Peukert equation for battery capacity modeling through inclusion of a temperature dependency. *Journal of Power Sources*, 235:148–158, 2013.

[58] Alberto Bocca, Alberto Macii, Enrico Macii, and Massimo Poncino. Composable battery model templates based on manufacturers' data. *IEEE Design & Test*, 35(3):66–72, 2018.

[59] Donkyu Baek et al. Battery-aware operation range estimation for terrestrial and aerial electric vehicles. *IEEE Transactions on Vehicular Technology*, 68(6):5471–5482, 2019.

[60] Swaminathan Narayanaswamy, Steffen Schlueter, Sebastian Steinhorst, Martin Lukasiewycz, Samarjit Chakraborty, and Harry Ernst Hoster. On battery recovery effect in wireless sensor nodes. *ACM Transactions on Design Automation of Electronic Systems (TODAES)*, 21(4):1–28, 2016.

[61] Laura Marie Feeney, Christian Rohner, Per Gunningberg, Anders Lindgren, and Lars Andersson. How do the dynamics of battery discharge affect sensor lifetime? In *2014 11th Annual Conference on Wireless On-demand Network Systems and Services (WONS)*, pages 49–56. IEEE, 2014.

[62] Vijay Raghunathan, Curt Schurgers, Sung Park, and Mani B. Srivastava. Energy-aware wireless microsensor networks. *IEEE Signal processing magazine*, 19(2):40–50, 2002.

[63] Philipp Mayer, Michele Magno, Thomas Brunner, and Luca Benini. LoRa vs. LoRa: In-field evaluation and comparison for long-lifetime sensor nodes. In *2019 IEEE 8th International Workshop on Advances in Sensors and Interfaces (IWASI)*, pages 307–311. IEEE, 2019.

[64] Christian Maurer, Walter Commerell, Andreas Hintennach, and Andreas Jossen. Capacity recovery effect in lithium sulfur batteries for electric vehicles. *World Electric Vehicle Journal*, 9(2):34, 2018.

[65] Daler Rakhmatov, Sarma Vrudhula, and Deborah A. Wallach. A model for battery lifetime analysis for organizing applications on a pocket computer. *IEEE transactions on very large scale integration (VLSI) systems*, 11(6):1019–1030, 2003.

[66] Mohsen Radfar, Amir Nakhlestani, Hoang Le Viet, and Aniruddha Desai. Battery management technique to reduce standby energy consumption in ultra-low power IoT and sensory applications. *IEEE Transactions on Circuits and Systems I: Regular Papers*, 67(1):336–345, 2020.

[67] Chi-Kin Chau, Fei Qin, Samir Sayed, Muhammad Husni Wahab, and Yang Yang. Harnessing battery recovery effect in wireless sensor networks: Experiments and analysis. *IEEE Journal on Selected Areas in Communications*, 28(7):1222–1232, 2010.

[68] Harneet Arora, Robert Simon Sherratt, Balazs Janko, and William Harwin. Experimental validation of the recovery effect in batteries for wearable sensors and healthcare devices discovering the existence of hidden time constants. *The Journal of Engineering*, 2017(10):548–556, 2017.

[69] Andreas Baumgardt, Florian Bachheibl, and Dieter Gerling. Utilization of the battery recovery effect in hybrid and electric vehicle applications. In *2014 17th International Conference on Electrical Machines and Systems (ICEMS)*, pages 254–260. IEEE, 2014.

[70] Carla-Fabiana Chiasserini and Ramesh R. Rao. A model for battery pulsed discharge with recovery effect. In *WCNC. 1999 IEEE Wireless Communications and Networking Conference (Cat. No. 99TH8466)*, volume 2, pages 636–639. IEEE, 1999.

[71] Jiucai Zhang, Song Ci, Hamid Sharif, and Mahmoud Alahmad. An enhanced circuit-based model for single-cell battery. In *2010 Twenty-Fifth Annual IEEE Applied Power Electronics Conference and Exposition (APEC)*, pages 672–675. IEEE, 2010.

[72] Energizer. Energizer E91 - Product Datasheet. https://data.energizer.com/pdfs/e91.pdf.

[73] Energizer. Energizer L91 - Product Datasheet. https://data.energizer.com/pdfs/l91.pdf.

[74] Energizer. Cylindrical Primary Lithium - Handbook and Application Manual. https://data.energizer.com/pdfs/lithiuml91l92_appman.pdf.

[75] Massimo Alioto. From less batteries to battery–Less alert systems with wide power adaptation down to nWs—Toward a smarter, greener world. *IEEE Design & Test*, 38(5):90–133, 2021.

[76] Alex S. Weddell, Michele Magno, Geoff V. Merrett, Davide Brunelli, Bashir M. Al-Hashimi, and Luca Benini. A survey of multi-source energy harvesting systems. In *2013 Design, Automation & Test in Europe Conference & Exhibition (DATE)*, pages 905–908. IEEE, 2013.

[77] F. Duffner, M. Wentker, M. Greenwood, and J. Leker. Battery cost modeling: A review and directions for future research. *Renewable and Sustainable Energy Reviews*, 127:109872, 2020.

[78] Paul A. Nelson, Shabbir Ahmed, Kevin G. Gallagher, and Dennis W. Dees. Modeling the performance and cost of lithium-ion batteries for electric-drive vehicles – third edition. Technical Report ANL/CSE-19/2, Argonne National Laboratory, March 2019.

[79] Xinfei Guo and Mircea R. Stan. *Circadian rhythms for future resilient electronic systems*. Springer, 2020.

[80] M. A. Hannan et al. Battery energy-storage system: A review of technologies, optimization objectives, constraints, approaches, and outstanding issues. *Journal of Energy Storage*, 42:103023, 2021.

[81] Iman Khajenasiri, Abouzar Estebsari, Marian Verhelst, and Georges Gielen. A review on Internet of Things solutions for intelligent energy control in buildings for smart city applications. *Energy Procedia*, 111:770–779, 2017.

[82] Jerome Peter Lynch. An overview of wireless structural health monitoring for civil structures. *Philosophical Transactions of the Royal Society A: Mathematical, Physical and Engineering Sciences*, 365(1851):345–372, 2007.

[83] Hasan Hayat, Thomas Griffiths, Desmond Brennan, Richard P. Lewis, Michael Barclay, Chris Weirman, Bruce Philip, and Justin R. Searle. The state-of-the-art of sensors and environmental monitoring technologies in buildings. *Sensors*, 19(17):3648, 2019.

[84] Hanjiro Ambrose and Alissa Kendall. Understanding the future of lithium: Part 1, resource model. *Journal of Industrial Ecology*, 24(1):80–89, 2020.

[85] Dominique Larcher and Jean-Marie Tarascon. Towards greener and more sustainable batteries for electrical energy storage. *Nature chemistry*, 7(1):19–29, 2015.

[86] F. Matthey, T. Kamijoh, K. Takeda, S. Ando, T. Nomura, T. Shibata, and A. Honzawa. Cost-benefit analysis tool and control strategy selection for lithium-ion battery energy storage system. In *2015 IEEE Power & Energy Society General Meeting*, pages 1–5. IEEE, 2015.

[87] Energizer. Alkaline Manganese Dioxide – Handbook and Application Manual. https://data.energizer.com/pdfs/alkaline_appman.pdf, 2018.

[88] Donkyu Baek, Alberto Bocca, and Alberto Macii. A cost of ownership analysis of batteries in all-electric and plug-in hybrid vehicles. *Energy, Ecology and Environment*, 7(6):604–613, 2022.

[89] © 2021 IEEE. Reprinted, with permission, from
Alberto Bocca, Alberto Macii and Enrico Macii. Forecasting the grid power demand of charging stations from EV drivers' attitude. In *2021 IEEE 45th Annual Computers, Software, and Applications Conference (COMPSAC)*, pages 1867–1872, 2021.

[90] Ana Carolina Rodrigues Teixeira and José Ricardo Sodré. Impacts of replacement of engine powered vehicles by electric vehicles on energy consumption on CO_2 emissions. *Transp. Research Part D: Transport and Environment*, 59:375–384, 2018.

[91] IEA - International Energy Agency. Global EV Outlook 2022. https://www.iea.org/reports/global-ev-outlook-2022, 2022.

[92] LMC Automotive Limited. Global Hybrid & EV Bulletin. https://lmc-auto.com/wp-content/uploads/2021/04/LMCA-G-HEVB-April-2021.pdf, 2021.

[93] G. Kalghatgi. Is it really the end of internal combustion engines and petroleum in transport? *Applied Energy*, 225:965–974, 2018.

[94] Björn Nykvist and Måns Nilsson. Rapidly falling costs of battery packs for electric vehicles. *Nature climate change*, 5(4):329–332, 2015.

[95] Xiao Shi, Jian Pan, Hewu Wang, and Hua Cai. Battery electric vehicles: What is the minimum range required? *Energy*, 166:352–358, 2019.

[96] Languang Lu, Xuebing Han, Jianqiu Li, Jianfeng Hua, and Minggao Ouyang. A review on the key issues for lithium-ion battery management in electric vehicles. *Journal of Power Sources*, 226:272–288, 2013.

[97] Matthieu Dubarry and Bor Yann Liaw. Development of a universal modeling tool for rechargeable lithium batteries. *Journal of Power Sources*, 174:856–860, 2007.

[98] Eduardo Redondo-Iglesias, Pascal Venet, and Serge Pelissier. Eyring acceleration model for predicting calendar ageing of lithium-ion batteries. *Journal of Energy Storage*, 13:176–183, 2017.

[99] EPA - United States Environmental Protection Agency. Vehicle and Fuel Emissions Testing. https://www.epa.gov/vehicle-and-fuel-emissions-testing/dynamometer-drive-schedules.

[100] California Environmental Protection Agency - Air Resources Board. California's Advanced Clean Cars Midterm Review - Appendix I: Alternative Credits for Zero Emission Vehicles and Plug-in Hybrid Electric Vehicles. https://ww2.arb.ca.gov/sites/default/files/2020-01/appendix_i_credit_alternative_2_ac.pdf, January 18 2017.

[101] George E. Blomgren. The development and future of lithium ion batteries. *Journal of the Electrochemical Society*, 164(1):A5019–A5025, 2017.

[102] Jeremy Neubauer, Kandler Smith, Eric Wood, and Ahmed Pesaran. Identifying and overcoming critical barriers to widespread second use of PEV batteries. Technical report, National Renewable Energy Lab. (NREL), Golden, CO (United States), 2015.

[103] Naoki Nitta, Feixiang Wu, Jung Tae Lee, and Gleb Yushin. Li-ion battery materials: present and future. *Materials today*, 18(5):252–264, 2015.

[104] Aden Seaman, Thanh-Son Dao, and John McPhee. A survey of mathematics-based equivalent-circuit and electrochemical battery models for hybrid and electric vehicle simulation. *Journal of Power Sources*, 256:410–423, 2014.

[105] Massimo Petricca, Donghwa Shin, Alberto Bocca, Alberto Macii, Enrico Macii, and Massimo Poncino. An automated framework for generating variable-accuracy battery models from datasheet information. In *Proc. International Symposium on Low Power Design (ISLPED)*, pages 365–370, 2013.

[106] Alan Millner. Modeling lithium ion battery degradation in electric vehicles. In *Proc. IEEE Conference on Innovative Technologies for an Efficient and Reliable Electricity Supply (CITRES)*, pages 349–356, 2010.

[107] Tugce Yuksel and Jeremy Michalek. Evaluation of the effects of thermal management on battery life in plug-in hybrid electric vehicles. In *Proc. Society of Automotive Engineers World Congress*, 2012.

[108] Alberto Bocca, Alessandro Sassone, Alberto Macii, Enrico Macii, and Massimo Poncino. An aging-aware battery charge scheme for mobile devices exploiting plug-in time patterns. In *Proc. 33rd IEEE International Conference on Computer Design (ICCD)*, pages 407–410. IEEE, 2015.

[109] EPA - United States Environmental Protection Agency. EPA Urban Dynamometer Driving Schedule (UDDS). https://www.epa.gov/emission-standards-reference-guide/epa-urban-dynamometer-driving-schedule-udds.

[110] Michael Duoba, Henning Lohse-Busch, and Eric Rask. Evaluating plug-in vehicles (plug-in hybrid and battery electric vehicles) using standard dynamometer protocols. *World Electric Vehicle Journal*, 5(1):196–209, 2012.

[111] Y. Chen, K. Hu, Jing Zhao, G. Li, J. Johnson, and J. Zietsman. In-use energy and CO_2 emissions impact of a plug-in hybrid and battery electric vehicle based on real-world driving. *International Journal of Environmental Science and Technology*, 15(5):1001–1008, 2018.

[112] Hewu Wang, Xiaobin Zhang, and Minggao Ouyang. Energy consumption of electric vehicles based on real-world driving patterns: A case study of Beijing. *Applied energy*, 157:710–719, 2015.

[113] Steffen Bubeck, Jan Tomaschek, and Ulrich Fahl. Perspectives of electric mobility: Total cost of ownership of electric vehicles in Germany. *Transport Policy*, 50:63–77, 2016.

[114] Patrick M. Bösch, Felix Becker, Henrik Becker, and Kay W. Axhausen. Cost-based analysis of autonomous mobility services. *Transport Policy*, 64:76–91, 2018.

[115] T. Markel, A. Brooker, T. Hendricks, V. Johnson, and K. Kelly. ADVISOR: a systems analysis tool for advanced vehicle modeling. *Journal of Power Sources*, 2002.

[116] U.S. plug-in electric vehicle sales by model. Alternative Fuels Data Center, U.S. Department of Energy. https://afdc.energy.gov/data/10567, 2020.

[117] Zijian Huang, Shunnan Qi, and Zelei Sun. Analysis tesla in the future by binary option and four different sensitivity. In *2022 7th International Conference on Financial Innovation and Economic Development (ICFIED 2022)*, pages 683–688. Atlantis Press, 2022.

[118] Tesla, Inc. Tesla Model 3 Specs. https://www.tesla.com/model3.

[119] Toyota Motor Sales, U.S.A., Inc. Toyota Prius Specs. https://www.toyota.com/prius.

[120] GlobalPetrolPrices.com. Electricity Prices. https://www.globalpetrolprices.com.

[121] CNN Money. Gas Prices around the World. https://money.cnn.com/pf/features/lists/global_gasprices/.

[122] Tesla, Inc. Vehicle warranty. https://www.tesla.com/support/vehicle-warranty.

[123] Teng Zeng, Hongcai Zhang, and Scott Moura. Solving overstay and stochasticity in PEV charging station planning with real data. *IEEE Transactions on Industrial Informatics*, 16(5):3504–3514, 2020.

[124] Jeremy Neubauer and Eric Wood. The impact of range anxiety and home, workplace, and public charging infrastructure on simulated battery electric vehicle lifetime utility. *Journal of Power Sources*, 257:12–20, 2014.

[125] H. S. Das, M. M. Rahman, S. Li, and C. W. Tan. Electric vehicles standards, charging infrastructure, and impact on grid integration: A technological review. *Renewable and Sustainable Energy Reviews*, 120:109618, 2020.

[126] Filipe Joel Soares, P. M. Rocha Almeida, and J. A. Peças Lopes. Quasi-real-time management of electric vehicles charging. *Electric Power Systems Research*, 108:293–303, 2014.

[127] Monica Alonso, Hortensia Amaris, Jean Gardy Germain, and Juan Manuel Galan. Optimal charging scheduling of electric vehicles in smart grids by heuristic algorithms. *Energies*, 7(4):2449–2475, 2014.

[128] Xiaolin Ge, Liang Shi, Yang Fu, S. M. Muyeen, Zhiquan Zhang, and Hongbo He. Data-driven spatial-temporal prediction of electric vehicle load profile considering charging behavior. *Electric Power Systems Research*, 187:106469, 2020.

[129] Yue Xiang, Zhuozhen Jiang, Chenghong Gu, Fei Teng, Xiangyu Wei, and Yang Wang. Electric vehicle charging in smart grid: A spatial-temporal simulation method. *Energy*, 189:116221, 2019.

[130] P. Zhang, K. Qian, C. Zhou, B. G. Stewart, and D. M. Hepburn. A methodology for optimization of power systems demand due to electric vehicle charging load. *IEEE Transactions on Power Systems*, 27(3):1628–1636, 2012.

[131] Md. Abdul Quddus, Omid Shahvari, Mohammad Marufuzzaman, John M. Usher, and Raed Jaradat. A collaborative energy sharing optimization model among electric vehicle charging stations, commercial buildings, and power grid. *Applied Energy*, 229:841–857, 2018.

[132] Zhile Yang, Kang Li, and Aoife Foley. Computational scheduling methods for integrating plug-in electric vehicles with power systems: A review. *Renewable and Sustainable Energy Reviews*, 51:396–416, 2015.

[133] Haiyang Lin, Kun Fu, Yu Wang, Qie Sun, Hailong Li, Yukun Hu, Bo Sun, and Ronald Wennersten. Characteristics of electric vehicle charging demand at multiple types of location-application of an agent-based trip chain model. *Energy*, 188:116122, 2019.

[134] Pol Olivella-Rosell, Roberto Villafafila-Robles, Andreas Sumper, and Joan Bergas-Jané. Probabilistic agent-based model of electric vehicle charging demand to analyse the impact on distribution networks. *Energies*, 8(5):4160–4187, 2015.

[135] Gonzalo Bustos-Turu, Koen H van Dam, Salvador Acha, and Nilay Shah. Estimating plug-in electric vehicle demand flexibility through an agent-based simulation model. In *IEEE PES Innovative Smart Grid Technologies, Europe*, pages 1–6, 2014.

[136] Wei Yang, Yue Xiang, Junyong Liu, and Chenghong Gu. Agent-based modeling for scale evolution of plug-in electric vehicles and charge demand. *IEEE Transactions on Power Systems*, 33(2):1915–1925, 2017.

[137] Uri Wilensky. NetLogo. http://ccl.northwestern.edu/netlogo/ Center for Connected Learning and Computer-Based Modeling, Northwestern University, Evanston, IL., 1999.

[138] Kalpesh Chaudhari, Nandha Kumar Kandasamy, Ashok Krishnan, Abhisek Ukil, and Hoay Beng Gooi. Agent-based aggregated behavior modeling for electric vehicle charging load. *IEEE Transactions on Industrial Informatics*, 15(2):856–868, 2019.

[139] Tobias Rodemann, Tom Eckhardt, René Unger, and Torsten Schwan. Using agent-based customer modeling for the evaluation of EV charging systems. *Energies*, 12(15):2858, 2019.

[140] Ye Shi, Hoang Duong Tuan, Andrey V. Savkin, Trung Q. Duong, and H. Vincent Poor. Model predictive control for smart grids with multiple electric-vehicle charging stations. *IEEE Transactions on Smart Grid*, 10(2):2127–2136, 2018.

[141] Martijn H. H. Schoot Uiterkamp, Marco E. T. Gerards, and Johann L. Hurink. Online electric vehicle charging with discrete charging rates. *Sustainable Energy, Grids and Networks*, 25:100423, 2021.

[142] Mariz B. Arias, Myungchin Kim, and Sungwoo Bae. Prediction of electric vehicle charging-power demand in realistic urban traffic networks. *Applied energy*, 195:738–753, 2017.

[143] M. Majidpour, C. Qiu, P. Chu, H. R. Pota, and R. Gadh. Forecasting the EV charging load based on customer profile or station measurement? *Applied Energy*, 163:134–141, 2016.

[144] Mushfiqur R Sarker, Hrvoje Pandžić, Kaiwen Sun, and Miguel A Ortega-Vazquez. Optimal operation of aggregated electric vehicle charging stations coupled with energy storage. *IET Generation, Transmission & Distribution*, 12(5):1127–1136, 2017.

[145] Yijia Cao, Shengwei Tang, Canbing Li, P. Zhang, Yi Tan, Zhikun Zhang, and Junxiong Li. An optimized EV charging model considering TOU price and SOC curve. *IEEE Transactions on Smart Grid*, 3(1):388–393, 2011.

[146] Alberto Bocca, Yukai Chen, Alberto Macii, Enrico Macii, and Massimo Poncino. Aging and cost optimal residential charging for plug-in EVs. *IEEE Design & Test*, 35(6):16–24, 2018.

[147] Yongmin Zhang, Pengcheng You, and Lin Cai. Optimal charging scheduling by pricing for EV charging station with dual charging modes. *IEEE Transactions on Intelligent Transportation Systems*, 20(9):3386–3396, 2018.

[148] Felix Tuchnitz, Niklas Ebell, Jonas Schlund, and Marco Pruckner. Development and evaluation of a smart charging strategy for an electric vehicle fleet based on reinforcement learning. *Applied Energy*, 285:116382, 2021.

[149] © 2022 IEEE. Reprinted, with permission, from
Alberto Bocca, Alberto Macii and Enrico Macii. A nonlinear two-parameter model for the spatial analysis of solar irradiation. In *2022 IEEE 46th Annual Computers, Software, and Applications Conference (COMPSAC)*, pages 1362–1367, 2022.

[150] Tanveer Ahmad and Huanxin Chen. Potential of three variant machine-learning models for forecasting district level medium-term and long-term energy demand in smart grid environment. *Energy*, 160:1008–1020, 2018.

[151] Daniel Scholten. The geopolitics of renewables—an introduction and expectations. In *The geopolitics of renewables*, pages 1–33. Springer, 2018.

[152] Luca Bergamasco and Pietro Asinari. Scalable methodology for the photovoltaic solar energy potential assessment based on available roof surface area: Application to Piedmont Region (Italy). *Solar Energy*, 85(5):1041–1055, 2011.

[153] Baran Yildiz, Jose I. Bilbao, and Alistair B. Sproul. A review and analysis of regression and machine learning models on commercial building electricity load forecasting. *Renewable and Sustainable Energy Reviews*, 73:1104–1122, 2017.

[154] Richard J. Brook and Gregory C. Arnold. *Applied regression analysis and experimental design*. Routledge, 2018.

[155] Jian Luo, Tao Hong, and Shu-Cherng Fang. Robust regression models for load forecasting. *IEEE Transactions on Smart Grid*, 10(5):5397–5404, 2018.

[156] Ioannis Antonopoulos, Valentin Robu, Benoit Couraud, Desen Kirli, Sonam Norbu, Aristides Kiprakis, David Flynn, Sergio Elizondo-Gonzalez, and Steve Wattam. Artificial intelligence and machine learning approaches to energy demand-side response: A systematic review. *Renewable and Sustainable Energy Reviews*, 130:109899, 2020.

[157] Vladimir Cherkassky and Yunqian Ma. Practical selection of SVM parameters and noise estimation for SVM regression. *Neural networks*, 17(1):113–126, 2004.

[158] Haitao Liu, Yew-Soon Ong, Xiaobo Shen, and Jianfei Cai. When Gaussian process meets big data: A review of scalable GPs. *IEEE Transactions on Neural Networks and Learning Systems*, 2020.

[159] Mahdi Sharifzadeh, Alexandra Sikinioti-Lock, and Nilay Shah. Machine-learning methods for integrated renewable power generation: A comparative study of artificial neural networks, support vector regression, and gaussian process regression. *Renewable and Sustainable Energy Reviews*, 108:513–538, 2019.

[160] Ahmad S. Ahmad, Mohammad Y. Hassan, Md. Pauzi Abdullah, Hasimah A. Rahman, F. Hussin, Hayati Abdullah, and Rahman Saidur. A review on applications of ANN and SVM for building electrical energy consumption forecasting. *Renewable and Sustainable Energy Reviews*, 33:102–109, 2014.

[161] A. K. Yadav and S. S. Chandel. Solar radiation prediction using Artificial Neural Network techniques: A review. *Renewable and sustainable energy reviews*, 33:772–781, 2014.

[162] Alexey Grigorevich Ivakhnenko. Polynomial theory of complex systems. *IEEE transactions on Systems, Man, and Cybernetics*, SMC-1(4):364–378, October 1971.

[163] Sung-Kwun Oh, Witold Pedrycz, and Byoung-Jun Park. Polynomial neural networks architecture: analysis and design. *Computers & Electrical Engineering*, 29(6):703–725, 2003.

[164] Olusola Samuel Ojo and Babatunde Adeyemi. Estimation of solar radiation using air temperature and geographical coordinate over Nigeria. *The Pacific Journal of Science and Technology*, 15(2):78–88, 2014.

[165] Jay Doorga, Soonil Rughooputh, and Ravindra Boojhawon. *Geospatial Optimization of Solar Energy: Cases from Around the World*. Springer Nature, 2022.

[166] Ling Tim Wong and Wan Ki Chow. Solar radiation model. *Applied Energy*, 69(3):191–224, 2001.

[167] Mawloud Guermoui, Farid Melgani, Kacem Gairaa, and Mohamed Lamine Mekhalfi. A comprehensive review of hybrid models for solar radiation forecasting. *Journal of Cleaner Production*, 258:120357, 2020.

[168] Alberto Bocca et al. Multiple-regression method for fast estimation of solar irradiation and photovoltaic energy potentials over Europe and Africa. *Energies*, 11(12):3477, 2018.

[169] T. Huld, R. Müller, and A. Gambardella. A new solar radiation database for estimating PV performance in Europe and Africa. *Solar Energy*, 86(6):1803–1815, 2012.

[170] European Commission - Joint Research Centre. PVGIS 5.2. https://joint-research-centre.ec.europa.eu/pvgis-photovoltaic-geographical-information-system/pvgis-releases/pvgis-52_en., 2022.

[171] European Commission - Joint Research Centre. Getting started with PVGIS - API Non-Interactive Service. https://joint-research-centre.ec.europa.eu/pvgis-photovoltaic-geographical-information-system/getting-started-pvgis/api-non-interactive-service_en., 2022.

[172] Mathworks. Regression Learner App. https://mathworks.com/help/stats/regression-learner-app.html.

Appendix A

MATLAB code for the PVGIS data extraction

```
clear all
close all
clc
path = 'saved_2/';

% Coordinates of the locations in Europe
E_coord = [59.98 30.46; 55.94 -3.30; 54.64 25.27; 52.54 13.52; 52.20 21.00; 52.06 4.36; 51.48 0.00; 50.86 4.37; 50.45 30.46;
50.13 8.70; 50.12 14.62; 48.91 2.37; 48.80 9.20; 48.17 16.39; 48.11 17.06; 47.47 19.15; 47.14 9.50; 46.99 28.84; 46.96 7.43;
46.47 11.32; 46.08 14.48; 45.81 15.97; 45.11 7.73; 44.80 20.38; 44.79 -0.53; 44.43 26.00; 43.83 18.34; 42.63 23.41; 42.42
19.26; 41.97 12.53; 41.36 19.80; 41.07 28.77; 40.35 -3.73; 40.16 44.52; 38.75 -9.15; 37.98 23.70; 37.38 -5.95; 37.20 14.95;
36.15 -5.35; 35.14 33.38];

% Coordinates of the locations in Africa
A_coord = [36.74 10.24; 36.70 3.10; 33.96 -6.87; 32.76 13.17; 29.74 31.38; 23.31 32.33; 18.48 -15.21; 15.27 39.17; 15.27
32.50; 15.27 -4.17; 13.66 -15.69; 13.39 -16.70; 12.05 42.74; 12.05 -1.64; 10.45 41.73; 10.45 7.36; 8.84 38.11; 8.84 15.41; 7.97
-11.76; 7.23 -5.68; 5.63 0.00; 4.31 18.52; 4.02 31.34; 4.02 10.45; 2.41 45.80; 0.80 32.95; 0.52 25.20; -2.14 30.56; -4.02 39.38;
-4.20 15.23; -8.84 33.24; -13.66 33.85; -13.66 15.69; -15.11 39.31; -15.27 27.50; -18.48 47.32; -18.48 30.42; -23.31 16.60;
-24.58 25.83; -29.74 25.85];

nE = size(E_coord,1);
nA = size(A_coord,1);

% Setting the pause time between queries
pause('on');
t = 1;

% Database queries
for i=1:nE

    url=strcat('https://re.jrc.ec.europa.eu/api/PVcalc?lat=',num2str(E_coord(i,1)),'&lon=',num2str(E_coord(i,2)),...
'&peakpower=176&loss=16&optimalinclination=1&mountingplace=free&outputformat=csv&browser=1');

    data_FS_PV = webread(url);

    filename = strcat('./saved_2/coord_',num2str(E_coord(i,1)),'_',num2str(E_coord(i,2)),'_FS_PV.mat');

    save(filename,'data_FS_PV');

    pause(t);
```

```
    url = strcat('https://re.jrc.ec.europa.eu/api/PVcalc?lat=',num2str(E_coord(i,1)),'&lon=',num2str(E_coord(i,2)),...
'&peakpower=176&loss=16&optimalinclination=1&mountingplace=building&outputformat=csv&browser=1');

    data_BI_PV = webread(url);

    filename = strcat('./saved_2/coord_',num2str(E_coord(i,1)),'_',num2str(E_coord(i,2)),'_BI_PV.mat');

    save(filename,'data_BI_PV');

    pause(t);

    % Monthly radiation and daily temperature (average per month)

    url = strcat('https://re.jrc.ec.europa.eu/api/MRcalc?lat=',num2str(E_coord(i,1)),'&lon=',num2str(E_coord(i,2)),...
'&usehorizon=1&optrad=1&mr_dni=1&avtemp=1&startyear=2010&endyear=2016&outputformat=csv&browser=1');

    data_MR = webread(url);

    filename = strcat('./saved_2/coord_',num2str(E_coord(i,1)),'_',num2str(E_coord(i,2)),'_MR.mat');

    save(filename,'data_MR');

    pause(t);
end
for i=1:nA

    url=strcat('https://re.jrc.ec.europa.eu/api/PVcalc?lat=',num2str(A_coord(i,1)),'&lon=',num2str(A_coord(i,2)),...
'&peakpower=176&loss=16&optimalinclination=1&mountingplace=free&outputformat=csv&browser=1');

    data_FS_PV = webread(url);

    filename = strcat('./saved_2/coord_',num2str(A_coord(i,1)),'_',num2str(A_coord(i,2)),'_FS_PV.mat');

    save(filename,'data_FS_PV');

    pause(t);

    url = strcat('https://re.jrc.ec.europa.eu/api/PVcalc?lat=',num2str(A_coord(i,1)),'&lon=',num2str(A_coord(i,2)),...
'&peakpower=176&loss=16&optimalinclination=1&mountingplace=building&outputformat=csv&browser=1');

    data_BI_PV = webread(url);

    filename = strcat('./saved_2/coord_',num2str(A_coord(i,1)),'_',num2str(A_coord(i,2)),'_BI_PV.mat');

    save(filename,'data_BI_PV');

    pause(t);

    % Monthly radiation and daily temperature (average per month)

    url = strcat('https://re.jrc.ec.europa.eu/api/MRcalc?lat=',num2str(A_coord(i,1)),'&lon=',num2str(A_coord(i,2)),...
'&usehorizon=1&optrad=1&mr_dni=1&avtemp=1&startyear=2010&endyear=2016&outputformat=csv&browser=1');

    data_MR = webread(url);

    filename = strcat('./saved_2/coord_',num2str(A_coord(i,1)),'_',num2str(A_coord(i,2)),'_MR.mat');

    save(filename,'data_MR');

    pause(t);
end

% Generating the data tables: five columns (i.e., lat, long, alt, Hy, T)
A = zeros(nE,5);
B = zeros(nA,5);
```

```
for i=1:nE
    filename_PV = strcat(path,'coord_',num2str(E_coord(i,1)),'_',num2str(E_coord(i,2)),'_FS_PV.mat');
    filename_MR = strcat(path,'coord_',num2str(E_coord(i,1)),'_',num2str(E_coord(i,2)),'_MR.mat');
    A(i,1) = E_coord(i,1); % latitude
    A(i,2) = E_coord(i,2); % longitude
    A(i,3) = E_obs(i,3); % altitude
    load(filename_MR);
    A(i,4) = sum(data_MR.T2m(73:84))/12; % monthly mean temperature
    load(filename_PV);
    A(i,5) = sum(data_FS_PV.H_i__m(1:12)); % Hy[kWh/m^2]: yearly irradiation
end

for i=1:nA
    filename_PV = strcat(path,'coord_',num2str(A_coord(i,1)),'_',num2str(A_coord(i,2)),'_FS_PV.mat');
    filename_MR = strcat(path,'coord_',num2str(A_coord(i,1)),'_',num2str(A_coord(i,2)),'_MR.mat');
    B(i,1) = A_coord(i,1); % latitude
    B(i,2) = A_coord(i,2); % longitude
    B(i,3) = A_obs(i,3); % altitude
    load(filename_MR);
    B(i,4) = sum(data_MR.T2m(73:84))/12; % monthly mean temperature
    load(filename_PV);
    B(i,5) = sum(data_FS_PV.H_i__m(1:12)); % Hy[kWh/m^2]: yearly irradiation
end

M = [A; B];
M_reg_Hy_2p = [M(:,1) M(:,4) M(:,5)]; % matrix for the Regression Learner
M_reg_Hy_3p = [M(:,1) M(:,3) M(:,4) M(:,5)]; % matrix for the Regression Learner
nM = size(M,1);
```

Appendix B

Table 5.1 and Table 5.2 report the full data sets of the locations in Europe and Africa, respectively.

The locations in Europe were selected from 33 different countries, in the latitude range from 33.38° to 59.98°, in the altitude range from 0 to 1011 m a.s.l., and the mean temperature range from 6.1 to 20.9 °C.

The locations in Africa were selected from 38 different countries, in the latitude range from -29.74° to 36.74°, in the altitude range from 0 to 2379 m a.s.l., and the mean temperature range from 14.5 to 30.6 °C.

Table 5.1 Locations in Europe with related geodata and the yearly solar irradiation H_y as obtained from the PVGIS tool [1] and the proposed model in (4.5). Each pair of coordinates refers to a place in a region where the mentioned location is generally the most representative.

Location	**Nation**	ϕ	λ	h	T_m	$H_y\ [kWh/m^2]$		Δ
		$[^\circ]$	$[^\circ]$	$[m\ asl]$	$[^\circ C]$	*PVGIS*	*model*	[%]
St. Petersburg	Russia	59.98	30.46	18	6.1	994	893	-10.2
Edinburgh	Scotland	55.94	-3.30	44	9.3	1025	1078	5.1
Vilnius	Lithuania	54.64	25.27	186	7.9	1153	1109	-3.9
Berlin	Germany	52.54	13.52	55	10.6	1261	1248	-1.0
Warsaw	Poland	52.20	21.00	110	9.5	1273	1228	-3.6
The Hague	Netherlands	52.06	4.36	0	11.6	1270	1302	2.5
London	England	51.48	0.00	28	11.2	1231	1308	6.2
Brussels	Belgium	50.86	4.37	54	11.1	1262	1325	5.0
Kiev	Ukraine	50.45	30.46	165	9.3	1356	1288	-5.0
Frankfurt	Germany	50.13	8.70	133	11.4	1304	1360	4.3
Prague	Czech Rep.	50.12	14.62	280	9.9	1319	1313	-0.4
Paris	France	48.91	2.37	38	11.0	1370	1388	1.3
Stuttgart	Germany	48.80	9.20	242	11.4	1368	1404	2.6
Vienna	Austria	48.17	16.39	223	11.0	1426	1412	-0.9
Bratislava	Slovakia	48.11	17.06	134	12.0	1466	1451	-1.0
Budapest	Hungary	47.47	19.15	123	11.3	1526	1443	-5.4
Vaduz	Liechtenstein	47.14	9.50	454	11.2	1352	1452	7.4
Chişinău	Moldova	46.99	28.84	123	11.5	1499	1466	-2.2
Bern	Switzerland	46.96	7.43	571	9.7	1480	1416	-4.4
Bolzano	Italy	46.47	11.32	238	12.7	1736	1530	-11.8
Ljubljana	Slovenia	46.08	14.48	311	12.0	1462	1512	3.4
Zagreb	Croatia	45.81	15.97	127	12.4	1513	1536	1.5
Turin	Italy	45.11	7.73	210	13.2	1725	1592	-7.7
Belgrade	Serbia	44.80	20.38	80	13.0	1568	1591	1.5
Bordeaux	France	44.79	-0.53	4	14.2	1594	1649	3.5
Bucharest	Romania	44.43	26.00	90	12.2	1613	1568	-2.8
Sarajevo	Bosnia-Herzeg.	43.83	18.34	514	11.3	1455	1553	6.8
Sofia	Bulgaria	42.63	23.41	575	11.6	1584	1597	0.8
Podgorica	Montenegro	42.42	19.26	48	17.2	1854	1872	0.9
Rome	Italy	41.97	12.53	54	17.7	1912	1916	0.2
Tirana	Albania	41.36	19.80	111	16.3	1870	1843	-1.5
Istanbul	Turkey	41.07	28.77	90	15.1	1718	1781	3.6
Madrid	Spain	40.35	-3.73	615	15.8	2111	1834	-13.1
Yerevan	Armenia	40.16	44.52	1011	11.1	1820	1648	-9.4
Lisbon	Portugal	38.75	-9.15	89	16.9	1994	1920	-3.7
Athens	Greece	37.98	23.70	30	18.7	2057	2043	-0.6
Seville	Spain	37.38	-5.95	14	18.7	2189	2046	-6.5
Syracuse	Italy	37.20	14.95	348	18.6	1937	2046	5.6
Gibraltar	Gibraltar	36.15	-5.35	4	18.8	2018	2069	2.6
Nicosia	Cyprus	35.14	33.38	171	20.9	2161	2214	2.4

Table 5.2 Locations in Africa with related geodata and the yearly solar irradiation H_y as obtained from the PVGIS tool [1] and the proposed model in (4.5). Each pair of coordinates refers to a place in a region where the mentioned location is generally the most representative.

Location	Nation	ϕ	λ	h	T_m	$H_y\ [kWh/m^2]$		Δ
		[°]	[°]	[*m asl*]	[°*C*]	*PVGIS*	*model*	[%]
Tunisi	Tunisia	36.74	10.24	16	19.5	2031	2111	3.9
Algiers	Algeria	36.70	3.10	12	19.5	2058	2113	2.7
Rabat	Morocco	33.96	-6.87	75	18.7	2177	2099	-3.6
Tripoli	Lybia	32.76	13.17	51	22.6	2258	2331	3.2
Cairo	Egypt	29.74	31.38	96	22.6	2487	2337	-6.0
Aswan	Egypt	23.31	32.33	240	27.5	2675	2567	-4.0
Nouakchott	Mauritania	18.48	-15.21	12	28.6	2463	2533	2.8
Asmara	Eritrea	15.27	39.17	1337	23.5	2226	2283	2.5
Karthoum	Sudan	15.27	32.50	379	30.6	2554	2532	-0.9
Mopti	Mali	15.27	-4.17	261	28.8	2428	2462	1.4
Kaolack	Senegal	13.66	-15.69	0	27.5	2337	2376	1.7
Banjul	Gambia	13.39	-16.70	21	25.1	2285	2300	0.6
Djibuti	Rep. of Djibuti	12.05	42.74	942	26.9	2394	2322	-3.0
Ouagadougou	Burkina Faso	12.05	-1.64	319	28.0	2345	2351	0.3
Dire Dawa	Ethiopia	10.45	41.73	677	28.8	2464	2328	-5.5
Kaduna	Nigeria	10.45	7.36	589	25.2	2258	2246	-0.5
Addis Ababa	Ethiopia	8.84	38.11	2379	14.5	2163	2099	-2.9
Moundou	Chad	8.84	15.41	420	27.4	2274	2251	-1.0
Bo	Sierra Leone	7.97	-11.76	86	24.8	1993	2185	9.6
Bouaflé	Côte d'Ivoire	7.23	-5.68	185	25.3	2028	2176	7.3
Accra	Ghana	5.63	0.00	9	26.4	2159	2147	-0.5
Bangui	Central Afr. Rep.	4.31	18,52	383	24.6	2035	2098	3.1
Juba	South Sudan	4.02	31.34	803	25.1	2135	2094	-2.0
Douala	Cameroon	4.02	10.45	327	24.6	1832	2091	14.1
Mogadishu	Somalia	2.41	45.80	32	27.2	2417	2057	-14.9
Kampala	Uganda	0.80	32.95	1075	22.1	2071	2013	-2.8
Kisangani	D.R. of the Congo	0.52	25.20	399	24.0	1876	2001	6.7
Kibungo	Rwanda	-2.14	30.56	1585	19.8	1858	2043	10.0
Mombasa	Kenya	-4.02	39.38	219	24.0	2082	2088	0.3
Brazzaville	Rep. of the Congo	-4.20	15.23	377	24.1	1843	2092	13.5
Mbeya	Tanzania	-8.84	33.24	1261	21.0	2150	2148	-0.1
Lilongwe	Malawi	-13.66	33.85	1438	18.7	2106	2157	2.4
Huambo	Angola	-13.66	15.69	1562	20.3	2169	2188	0.9
Nampula	Mozambique	-15.11	39.31	388	23.6	2086	2285	9.5
Lusaka	Zambia	-15.27	27.50	1030	22.1	2191	2245	2.5
Antananarivo	Madagascar	-18.48	47.32	1392	17.4	2113	2143	1.4
Harare	Zimbabwe	-18.48	30.42	1281	21.0	2194	2238	2.0
Windhoek	Namibia	-23.31	16.60	1794	20.1	2301	2220	-3.5
Gaborone	Botswana	-24.58	25.83	1015	22.1	2147	2304	7.3
Bloemfontein	South Africa	-29.74	25.85	1411	17.1	2103	2068	-1.7